



Damage Development in Neutron-Irradiated Concrete in a Test Reactor: Hygro-Thermal and Mechanical Simulations

January 2021

Changing the World's Energy Future

Naman Saklani, Gaurav Banwat, Benjamin W Spencer, Subramaniam Rajan, Gaurav Sant, Narayanan Neithalath



DISCLAIMER

This information was prepared as an account of work sponsored by an agency of the U.S. Government. Neither the U.S. Government nor any agency thereof, nor any of their employees, makes any warranty, expressed or implied, or assumes any legal liability or responsibility for the accuracy, completeness, or usefulness, of any information, apparatus, product, or process disclosed, or represents that its use would not infringe privately owned rights. References herein to any specific commercial product, process, or service by trade name, trade mark, manufacturer, or otherwise, does not necessarily constitute or imply its endorsement, recommendation, or favoring by the U.S. Government or any agency thereof. The views and opinions of authors expressed herein do not necessarily state or reflect those of the U.S. Government or any agency thereof.

Damage Development in Neutron-Irradiated Concrete in a Test Reactor: Hygro-Thermal and Mechanical Simulations

**Naman Saklani, Gaurav Banwat, Benjamin W Spencer, Subramaniam Rajan,
Gaurav Sant, Narayanan Neithalath**

January 2021

**Idaho National Laboratory
Idaho Falls, Idaho 83415**

<http://www.inl.gov>

**Prepared for the
U.S. Department of Energy
Under DOE Idaho Operations Office
Contract DE-AC07-05ID14517**

Damage Development in Neutron-Irradiated Concrete in a Test Reactor: Hygro-Thermal and Mechanical Simulations

Naman Saklani[†], Gaurav Banwat[‡], Benjamin Spencer[§], Subramaniam Rajan^{**}, Gaurav Sant^{††}, and Narayanan Neithalath^{‡‡}

This article is published as: N. Saklani, G. Banwat, B. Spencer, S. Rajan, G. Sant, and N. Neithalath. Damage development in neutron-irradiated concrete in a test reactor: Hygro-thermal and mechanical simulations. *Cement and Concrete Research*, 142:106349, January 2021.

<https://doi.org/10.1016/j.cemconres.2020.106349>

ABSTRACT

This paper reports the development of a 3D mesoscale hygro-thermal-mechanical simulation approach to predict damage in concrete irradiated in a test reactor. This framework, developed in MOOSE, considers the effects of elevated temperature, moisture content, and high neutron fluence (energy threshold, $E > 0.1$ MeV) on the mortar and aggregates separately. The first-stage simulation implements hygro-thermal analysis to determine the temperature and RH inside the specimen as a function of imposed radiation energy. These are used as inputs to the second stage, which considers radiation-induced volumetric expansion (RIVE) of aggregates, and creep, shrinkage, and stress-strain response of mortar to predict the expansion, stresses, and damage in specimens made using different coarse aggregates and subjected to different irradiation times. The irradiation time-dependent damage in the mortar is expressed using an isotropic damage parameter. This multi-physics model serves as a predictive tool for damage quantification in concrete due to neutron irradiation.

Keywords: Neutron irradiation; Finite element simulation; Radiation induced volumetric expansion; Damage; Elastic modulus

[†] Graduate student, School of Sustainable Engineering and the Built Environment, Arizona State University, Tempe AZ

[‡] Graduate student, School of Sustainable Engineering and the Built Environment, Arizona State University, Tempe AZ

[§] Computational Mechanics and Materials, Idaho National Laboratory, Idaho Falls, ID, USA

^{**} Professor, School of Sustainable Engineering and the Built Environment, Arizona State University, Tempe AZ

^{††} Professor and Henry Samueli Fellow, Department of Civil and Environmental Engineering, University of California Los Angeles, Los Angeles CA

^{‡‡} Professor, School of Sustainable Engineering and the Built Environment, Arizona State University, Tempe AZ; Corresponding Author (Narayanan.Neithalath@asu.edu; Phone: +1-480-965-6023; Fax: +1-480-965-0557)

Notations

Material Properties- Aggregates		<u>Creep model</u>	
	Thermal expansion coefficient of aggregate		Elasticity of standalone and Kelvin Voigt spring
	Volume fraction of aggregate		Constant parameter for estimating viscosity
	Specific heat per unit mass of the aggregates		Viscosity of the standalone and Kelvin Voigt dashpot
	Coefficient in Bykov equation		Material parameter in creep model
	Maximum volumetric expansion observed in irradiation experiments		Activation temperature
	Radiation induced volumetric expansion (RIVE)	<u>Damage model</u>	
	Elastic modulus of aggregate		Parameter to control exponential softening
	Static elastic modulus of aggregate		
	Thermal conductivity		Isotropic damage index
	Fast neutron fluence when expansion is half of the maximum expansion		Elastic and creep strain
		, , and	Second order stress and elastic strain tensors, and fourth-order elasticity tensor
	Pulse velocity		Fracture energy
	Aggregate density		Characteristic length
Material Properties- Mortar			State variable
	Thermal expansion coefficient of mortar		Initial strain at cracking
	Elastic modulus of mortar		Compressive-tensile strength ratio
	Linear drying shrinkage		Poisson's ratio of mortar
	Free shrinkage coefficient	Other/common parameters	
	Pore relative humidity		Coefficient of thermal expansion and volumetric ratio of sand in mortar.
<u>Coupled hygro-thermal model</u>			
	Parameters used in the definition of	,	TEC and bulk modulus of cement paste
	Specific heat per unit mass of mortar		Heat transfer coefficient
	Heat capacity of free water		Humidity
	Isobaric heat capacity of water		Ambient humidity
	GAB model parameters		Surface humidity
	Moisture capacity		Thermal strain
	Moisture diffusivity		Fast neutron fluence
	Diffusion coefficient of HCP		Time
	Volume fraction of fine aggregate		Temperature
	Moisture flux		Reference temperature
	Thermal conductivity of mortar		Ambient temperature
	Mortar density		Surface temperature of aggregate or mortar
	Total water content		Rate of deposited energy
	Free evaporable water released into the pores		Water-to-cement ratio
	Quantity of vapor absorbed at 100% humidity		Elastic modulus of concrete
			Bulk modulus of concrete

1 INTRODUCTION

Nuclear power plants are generally licensed in the U.S. for up to 40 years of operation [1]. These licenses can be renewed for 20 years by the U.S. Nuclear Regulatory Commission (NRC) if there is reasonable confidence in continued safe operation. Due to the high capital costs of nuclear power plant construction and decommissioning, the possibility of extending the operating life of existing reactors has been one of the leading points of discussion in the nuclear industry [2,3]. This has renewed interest in understanding the structural integrity of the concrete biological shield and the corresponding degradation mechanisms of concrete under prolonged exposure to neutron and gamma radiation. The primary support structure for the reactor pressure vessel is also made of concrete and is exposed to radiation throughout its operation. This irradiation can result in severe cracking and damage in the concrete, potentially impacting its structural capacity and ability to perform its shielding function. It has been reported that neutron irradiation has a significantly larger influence on tensile strength than the compressive strength of concrete [4].

It is now well-recognized that radiation-induced volumetric expansion (RIVE) of aggregates is the primary mechanism responsible for the degradation and consequent loss of properties of concrete subjected to neutron radiation [3–6]. When neutrons interact with concrete, they tend to change the lattice spacing of the interfering atoms in the crystal structure and, thus, more strongly influence the densely packed structure in aggregates than the porous cement paste, which has a random structure [3,7–11]. It has also been observed that siliceous aggregates are more susceptible to irradiation and consequent metamictization (radiation-induced amorphization) than carbonate aggregates. The change in alignment of silicate tetrahedrons that leads to the atomic bond stretching and breaking is reported to be responsible for damage [7–13]. This is a result of covalent bonding in quartz; during neutron collisions, covalent bonds sustain permanent deformations due to their inherent inability to recrystallize, in contrast to ionic bonds [4,5,14–17].

Radiation impacts a multitude of complex mechanisms that need to be considered while developing numerical models to predict radiation-induced damage in concrete. Gamma radiation is experienced in conjunction with neutron irradiation. The gamma-ray dosages in the structural components of interest are generally not sufficient to cause metamictization of aggregates; however, they can cause radiolysis of water present in the hardened cement paste [5,17,18]. The gamma rays are ultimately converted to heat in a process referred to as gamma heating and cause volume changes due to loss of water from the specimen. The elevated temperature also likely has a healing effect that is reported to reduce RIVE [14]. The changes in temperature and moisture conditions inside the specimen influence the rate of shrinkage

and creep [19–21]. All these factors could vary between test reactors and the actual in-service conditions present in a light water reactors (LWRs).

Numerical models describing irradiated concrete performance are limited. One of the first models on irradiated concrete is attributed to Pomaro et al. [22,23], who considered a thermo-hygro-radiation model coupled with a viscoelastic-damage model on a homogenized concrete specimen. This robust model satisfactorily represented the temperature change and damage in the specimen exposed to radiation. This study was further extended to the mesoscale by Salomoni et al. [24]. However, both these approaches did not account explicitly for RIVE, which could be as high as 18% for aggregates with high quartz content [25,26]. The model also did not consider the effects of high temperature on diffusivity, adsorption isotherm and creep, which results in a response that is different from that at room temperature [27–29]. A micromechanical model to evaluate the role of aggregate RIVE and its impact on damage of concrete was put forth by Le Pape et al. [30]. Giorla et al. [15] developed an irradiated concrete 2D mesoscale model to simulate the experimental data published by Elleuch et al. [6] in 1972. Though RIVE is considered in this model, the model does not account for thermal and moisture transport through the specimen under irradiation conditions. Models that account for one-dimensional thermo-radiation transport to predict the neutron fluence and temperature profile inside a concrete biological shield wall [31], and to evaluate the material strength degradation, considering heat, moisture and radiation transport coupled with cement hydration [32], have also been proposed.

The three-dimensional (3D) mesoscale behavioral finite element framework developed in the MOOSE framework [33–35], implemented in this work, accounts for RIVE and carries out hygro-thermal and mechanical simulations separately at every time step. A 3D mesoscale model is created to simulate RIVE of elastic aggregates and the corresponding damage propagation in the paste undergoing creep, thermal strains, and drying shrinkage. The use of a 3D model was necessitated by the fact that a 2D model cannot capture certain geometrical effects, and could also lead to over estimation of crack-bridging and consequently lead to premature estimation of failure in the specimen [36]. The framework considers the effect of elevated temperature, moisture content, and high neutron fluence on the mortar and aggregates separately. There is a dearth of information in the open literature on the properties of concrete under irradiation. The limited tests, whenever available, correspond to different radiation exposure and dosages, concrete mixtures, aggregate types, and curing ages, which makes accurate simulations difficult [4,30]. However, it is well known that the mechanical properties (modulus, tensile strength etc.) and its behavior (creep, shrinkage etc.) are highly dependent on the temperature and moisture conditions. As we will see later in the sections, these properties can vary greatly inside the

specimen, especially as thickness of the specimen increases. In 2017, Maruyama et al. [5] published a detailed study, spanning eight years, on the influence of neutron and gamma irradiation and the corresponding effects of heating and drying on concrete at the JEEP II test reactor at Norway's Institute for Energy Technology. JEEP II is well suited for concrete irradiation tests because it has low levels of gamma heating in proportion to fast-neutron flux levels with a neutron flux of 2×10^{12} n/cm²/s and gamma heating restricted to 0.04 W/g [5]. This dataset, which to-date, is among the most comprehensive sets of experimental results on irradiated concrete in a test reactor, is used in the simulation exercise reported in this paper. The high neutron fluence causes metamictization and RIVE in the aggregates that are much larger than those observed during thermal expansion or alkali-silica reaction [5,15]. Using released-gas measurements and water-vapor sorption isotherms, the pore humidity in the concrete is also estimated. Although the effect of irradiation on creep is not well understood, the effects of elevated temperature and humidity on creep are well known and are considered in the present framework. We have carried out the simulations in two stages. In Stage 1, coupled hygro-thermal analysis [37–39] is carried out to ascertain the temperature and humidity conditions inside the specimen under irradiation. The temperature and humidity profiles from these simulations form the inputs for Stage 2 simulations, where these fields are used to compute the strains and corresponding stresses and damage in the specimen. The framework presented here acts as a predictive tool to determine the microscale damage and macroscale expansion in concrete due to neutron irradiation and can be extended to calculate the overall structural deterioration.

2 SIMULATION APPROACH

A two-stage simulation approach is used in this work as shown in Figure 1 [40]. Stage 1 consists of a coupled hygro-thermal model [37–39] to compute the temperature and relative humidity (RH) fields, which, together with the radiation field, form the input for Stage 2 simulations that consists of stress analysis and damage. The applied temperature, and moisture contents and pore RH profiles are calculated based on the energy deposited during irradiation in Stage 1. These fields are then applied to estimate creep, shrinkage and thermal strains on the mortar and RIVE on the aggregates in Stage 2, which are then converted to stress fields using the appropriate constitutive law. Even with such a comprehensive experimental data set as reported in [5], there are gaps that necessitate approximations or the use of models pertaining to non-irradiated concrete to provide reasonably accurate inputs to the simulations. They are explained wherever appropriate in this paper.

2.1 Experimental Inputs to Simulations from Maruyama et al. [5]

This section provides a brief summary of the experiments carried out by Maruyama et al. [5] to evaluate the reference values for fast-neutron fluence and gamma-ray dosage beyond which concrete is no longer considered structurally sound. Presently, these values are taken as 1×10^{20} n/cm² and 2×10^5 kGy respectively, based on the experimental studies on irradiated concrete by Hilsdorf et al. [41]. In a neutron-irradiation environment, secondary gamma rays are always present, which cause gamma heating. Thus, tests were carried out to ascertain the effect of neutrons, which were supplemented with tests to ascertain the effects of gamma rays on heating and drying of concrete. Two tests called interaction tests (IT) and physical-property tests (PPT) were carried out in [5]. The former deals with radiolysis of water in the hardened cement paste while the latter deals with changes in the properties such as Young's modulus and strength of the concrete, paste, and aggregate. PPTs also included heating and drying of specimens not exposed to radiation, to isolate the effects of other factors.

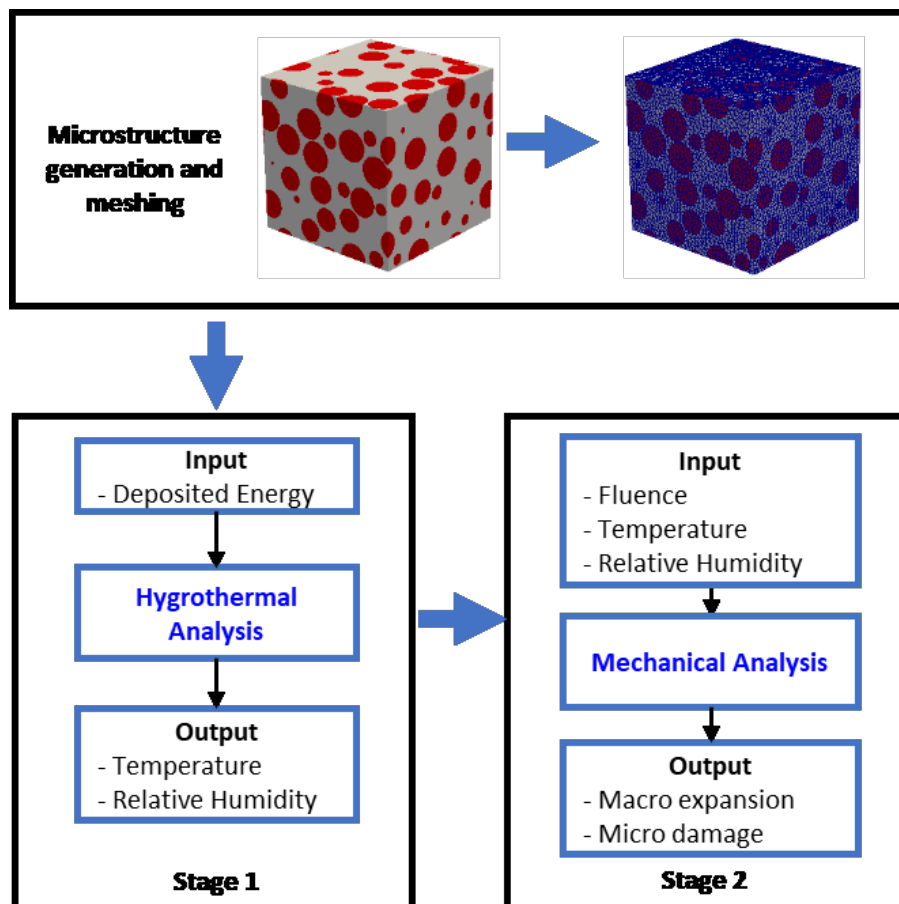


Figure 1: Meso-structural finite element (FE) framework to simulate damage in concrete subjected to neutron radiation. The meso structure and mesh generation for the current work is elaborated in

Section 2.2 while the constitutive model for Stage 1 and Stage 2 analysis along with the boundary conditions are elaborated later in Sections 2.3, 2.4 and 2.5 respectively.

In the experiments reported in [5], cylindrical concrete specimens 40 mm in diameter and 60 mm long, consisting of 5-13 mm sized coarse aggregates were used. The small diameter was required to reduce the confounding effects of gamma heating and a wider internal-temperature distribution. The samples for irradiation were placed in a double-tube aluminum capsule and loaded into the JEEP II Reactor. Several samples were placed simultaneously in the same capsule. The capsules were outfitted with fluence-monitoring wires, a gamma thermometer, and thermocouples. High early-strength cement with a water-to-cement ratio (w/c) of 0.50 was used to avoid the effects of hydration-induced strength development after the preparation period of one year during which the concrete and paste specimens were kept in a sealed condition at 20°C. The cement paste specimens were then dried at 75°C in the thermostatic chamber for 1 week. To evaluate the expansion level of aggregates containing α -quartz, irradiation tests were performed with five kinds of siliceous rocks (labeled as GA, GB, GC, GD, and GE in the order of decreasing quartz content; GA was an altered tuff with the highest quartz content and GE, a felsic sandstone).

Four concrete specimens (labeled CON-A) made using GA aggregate and four specimens (labeled CON-B) made using GB aggregate were used for the irradiation experiments. The concrete specimens were prepared using a w/c of 0.50, a cement content of 350-360 kg/m³ and coarse- and fine-aggregate contents of approximately 1000 and 800 kg/m³ respectively. Thus, the only major difference in the concretes used in the experiments (which are simulated in this paper) is the aggregate type. In addition, six cement paste specimens (10 mm diameter \times 10 mm long) and six aggregate specimens (10mm diameter \times 10 mm long) belonging to each type were also irradiated by placing them in the capsules in the irradiation chamber. The specimens were irradiated simultaneously at four levels of initial target neutron fluence - i.e., 0.75, 1.5, 3 and 10 ($\times 10^{19}$ n/cm² with $E > 0.1$ MeV) at a dosage of approximately 3.6×10^{12} n/cm²/s. The aforementioned levels of neutron fluence were achieved in approximately 30, 50, 155 and 320 days respectively, and are referred to as PPT-B, PPT-C, PPT-D, and PPT-E [5]. The number of days required to achieve the same fluence level varied slightly over the different experiments. The downside of a very high fluence level was that the results for PPT-E are not reliable as the specimen expanded more than expected, causing the fracture of the capsule holding the specimens and flooding by cooling water. Hence, the experimental results up to 155 days of irradiation (PPT-D) will only be considered reliable here. Table 1 summarizes the key experimental observations based on this

detailed study.

Table 1: Summary of experimental results by Maruyama et al. [5]

Neutron Irradiation Test	
PPT- Concrete (Specimens irradiated with four level of neutron fluence 0.75, 1.5, 3 and 6 ($\times 10^{19}n/cm^2$))	
Length change	Greater for Con-A (1% at highest fluence) than Con-B (0.5% at highest fluence) due to the higher amount of quartz in CON-A.
Strength	45% and 35% reduction in strength for CON-A and CON-B respectively.
Elastic modulus	70% and 60% reduction in elastic modulus for CON-A and CON-B respectively.
Cold Test- Concrete (not exposed to radiation; used for basic material properties)	
Compressive Strength	Observed to be constant at 70 MPa after 0, 50, 155 and 1000 days at 20°C beyond the sealed curing duration of one year for both concrete types. The 28-day compressive strength was 50 MPa.
Young's Modulus	35 GPa after 0, 50 and 155 days beyond the sealed curing duration of one year for both concrete types.
Heating Test- Concrete (Specimens heated at average and maximum temperatures as observed during PPT tests. Specimens not exposed to radiation; used for basic material properties)	
Shrinkage	Approximately 500 $\mu\epsilon$ at the end of 155 days.
Strength	~ 15% reduction in strength at the end of 155 days.
Modulus	~ 20% reduction in modulus at the end of 155 days.
IT-Cement paste (Specimens with varying curing conditions exposed to neutron radiation for approximately 2 months)	
Water Released	Specimens cured at saturated conditions released a significant amount moisture while specimens treated at 70° and 120° C before irradiation released no water.
PPT-Cement paste	
Length change	Initially, the specimens absorbed moisture and exhibited swelling; however, starts shrinking at higher fluence. Data is unreliable.
Vickers Hardness	Increased with fluence, indicating cement paste has high resistance against radiation.
PPT-Aggregates	
Volume change	5% and 13% change in volume for GA while 3% and 9 % change in volume for GB at the end of 155 and 320 days, respectively.
XRD data	Diffraction peaks grew smaller and shifted to the small angle region with increasing fluence, indicating structural collapse and widened atomic spacing.

2.2 Mesostructure and Mesh Generation

The 3D mesostructure for finite element simulations was generated based on the particle-size distribution (PSD) of the coarse aggregates used in the experimental work. A Lubachevsky-Stillinger algorithm is used to create the virtual mesostructure [42]. A cubical representative volume element (RVE) is first created in which hard particles are randomly distributed without allowing for particle overlapping. The particles are given random initial velocities and zero initial radius. An iterative

procedure is employed by which the particles collide, change position, and grow in the bounding box. The radius of any particle in the next event depends upon the growth rate which is set to match the actual PSD. A cylindrical specimen was then extracted from the cubical RVE. This will avoid wall effect in the simulations and thus does not account for the excessive cracking at the surface as was seen in the experiments (e.g., shown in [5]). Although surface cracking is undesirable, it is unlikely to have a major effect on the determination of homogenized damage (or homogenized elastic modulus) and the expansion of the concrete specimen, which are sought as validation parameters in this paper. Only two sizes of aggregates were used (i.e., 10 and 5 mm) in the simulations. The positions of the aggregates are kept the same from one simulation to another to avoid random scatter in the simulation results. A geometry adaptive meshing scheme [43] was implemented to generate 378,589 four-noded tetrahedral elements. This meshing technique adaptively controls the mesh size based on the local geometry. For example, a high-curvature region (e.g., around a particle) will have a finer mesh size when compared to a region with low curvature. A coarse-aggregate volume fraction of 0.32 was achieved using this method, compared to the value of 0.38 used in the experiments, as many smaller-sized aggregates were neglected. The finite element model and mesh are shown in Figure 2.

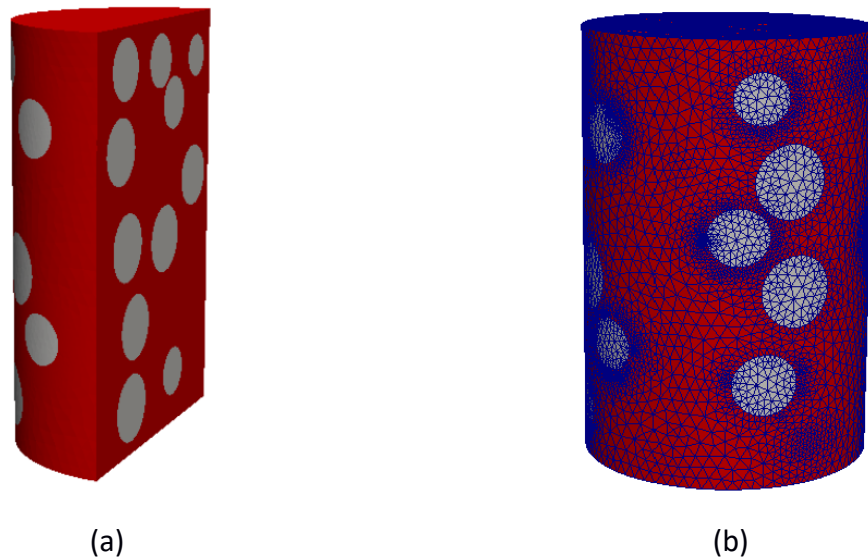


Figure 2: (a) Finite element model, and (b) geometry adaptive mesh used in the analysis. Note the refinement of the mesh around the aggregate-mortar interface. The model has 68,945 nodes and 378,589 four-noded tetrahedral elements.

2.3 Material Models for Stage 1 Analysis

This section describes the constitutive model used for Stage 1 analysis that computes the temperature and humidity conditions inside the specimen during irradiation. A schematic representation of the

simulation is shown in Figure 3. It is well known that the coarse aggregates do not shrink and creep as much as mortar. The maximum free linear shrinkage of aggregates GA and GB were approximately 50 $\mu\text{m}/\text{m}$ and 300 $\mu\text{m}/\text{m}$ [5]. This corresponds to a maximum volumetric shrinkage of 150 and 900 $\mu\text{m}/\text{m}$. This is more than two orders of magnitude smaller than the RIVE. Hence, the creep and shrinkage associated with aggregates are ignored (even though aggregates show some volume change) in the Stage 2 analysis, along with the moisture transport in the aggregates. However, temperature influences the RIVE of the aggregates and their thermal expansion, and thus the temperature rise in the aggregates due to irradiation is computed. The governing constitutive equations for the aggregates and mortar are described in the following sections.

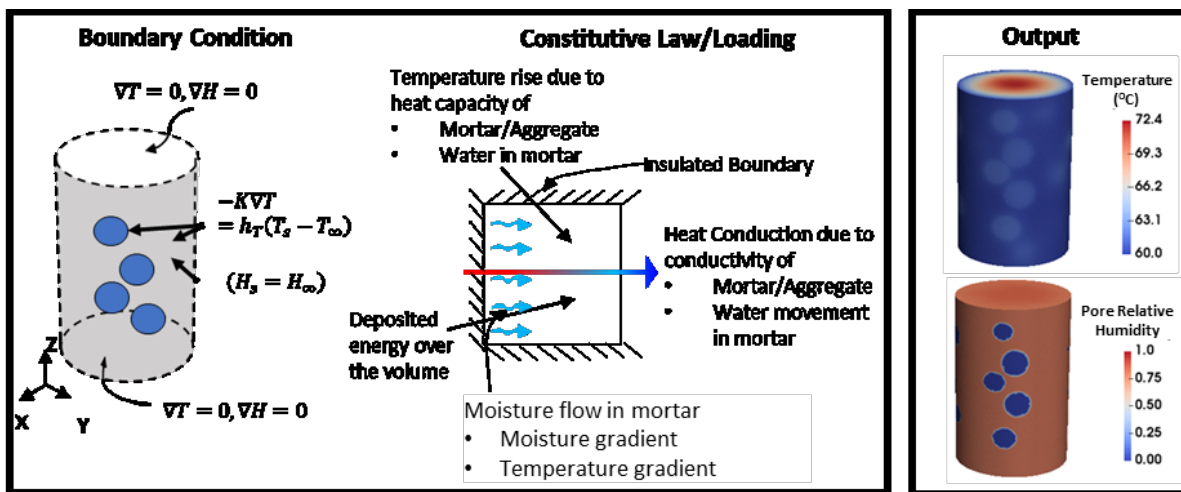


Figure 3: Schematic representation of constitutive law for hygrothermal analysis

2.3.1 Aggregate

Aggregates are assumed to conduct heat but are considered not to facilitate moisture transfer. The governing equation is given by the first law of thermodynamics (i.e., conservation of energy) as:

where T is the temperature, ρ is the aggregate density, and c_p is the specific heat (per unit mass) of the aggregates. \dot{Q} represents the rate of heat supplied by thermal conduction, where k is the thermal conductivity of the aggregate, and E is the deposited energy.

2.3.2 Mortar

It is difficult to estimate the humidity in the specimen during irradiation as no pore humidity measurements were carried out in the tests reported by [5], and no empirical models are currently

available. However, the effect of high temperature and its influence on humidity are considered in this study through a coupled moisture and heat-transfer model [37–39]. This model accounts for energy and mass balance in a capillary porous solid. Using energy equivalence, the heat equation was modified and is stated as [37]:

represents the heat consumed due to the change in temperature per unit volume per unit time, with being the density, the specific heat (per unit mass) of the mortar, and the temperature. represents rate of heat supplied by thermal conduction where is the thermal conductivity of the mortar. represents the convective heat transport due to water movement, with being the isobaric heat capacity of water (is the temperature in °C), and is the moisture flux. represents the heat flow due to adsorption of free water. represents the volumetric heat source. The thermal capacity and conductivity of mortar are assumed to be constant as these do not change appreciably below 100°C [44]. Using mass equivalence, the governing equation for moisture diffusion in mortar is given by,

where is the total water content, is the pore RH, is the moisture diffusivity, and is the total mass of free evaporable water released into the pores by dehydration of the cement paste. Both moisture capacity, and moisture diffusivity, depend on which makes this equation highly nonlinear. is ignored in this simulation as it was observed that only 1-2% of chemically bound water was released in IT experiments reported in [5]. This is not surprising given the temperatures registered within the specimens (60-72°C). The moisture diffusivity is a complex function of temperature, RH, and the pore structure of the material. There are indeed various diffusion mechanisms taking place simultaneously due to the different sizes of the pores in the hydrated cement paste. Kunzel [45] proposed a diffusion model that combined pressure-difference induced water-vapor diffusion, liquid-water diffusion through micropores and capillary pores, and moisture diffusion due to the gradient in RH in larger pores. Most models for cementitious materials, however, being empirical in nature, do not explicitly account for the different diffusion mechanisms, and tend to reproduce the overall trend. This includes the use of an S-shaped curve [46] and an exponential curve [47] that describe the diffusion coefficient in terms of RH in the pores. The S-shaped Bazant and Najjar model [46] was later expanded to include the effect of temperature [38] and w/c [27,28], and is used in the current work. These relationships which were developed for cement paste, are upscaled for mortar to include the effect of sand particles by multiplying with a function of the volume fraction of fine aggregate as suggested in [48].

where D is the diffusion coefficient of the paste that depends on pore RH and w/c and is given as [27]:

where

f is a function that upscales the diffusion coefficient of cement paste to mortar using the volume fraction of fine aggregate V_f ,

and g are functions that depend on temperature and are given as:

and

where T_0 is the reference temperature. It should be noted that the effect of radiation on the diffusion coefficient is not considered due to the absence of data.

The moisture capacity, m_0 , can be considered to be constant if the RH lies between 0.2 and 1.0, and the temperature is around $\sim 20^\circ\text{C}$ [49]. This parameter can be obtained from experimental or empirical desorption isotherms. Multiple studies characterize the water-vapor sorption isotherms for cementitious materials [50–55]; however most of these studies are carried out at room temperature. A few studies that demonstrate the effect of temperature on cementitious materials conclude that temperature modifies the sorption isotherms as a lesser amount of water is adsorbed at equilibrium at higher temperature [56]. It is also reported that higher temperature modifies the first desorption for the concrete significantly; and thus, it should be considered in the simulations [50,56]. Many adsorption models are available in the literature. Among them, the GAB model [27,57–59] can be used for cementitious materials as it best fits the sorption isotherm over the whole range of RH. It is a three-parameter model and is given as:

where m_0 and m_∞ are the quantities of water vapor absorbed (g/g of dried cement paste) at 100% RH and at any other humidity level, respectively. k_1 , k_2 , and k_3 are the three parameters of the GAB model. m_0 is the mass of adsorbate required to cover the adsorbent with a single molecular layer. k_1 and k_2 are empirical constants.

This equation was fitted using experimental desorption isotherm of cement paste data with a w/c of 0.45 at temperatures ranging from 23°-80°C [50], and the following relations were obtained for the three parameters:

The samples used in the experiments in [50] were 170 days old, indicating that they were sufficiently hydrated and can be compared to the hydration levels of the irradiated specimens simulated here. Moreover, a modest increase of w/c ratio from 0.45 to 0.50 (as used in the irradiated specimens) is likely to only cause a negligible change in the slope of the desorption isotherm [50]; hence, the fitted equations can be used directly in our simulations. The fitted results using Equation 12 and the comparison with the experimental results are shown in Figure 4.

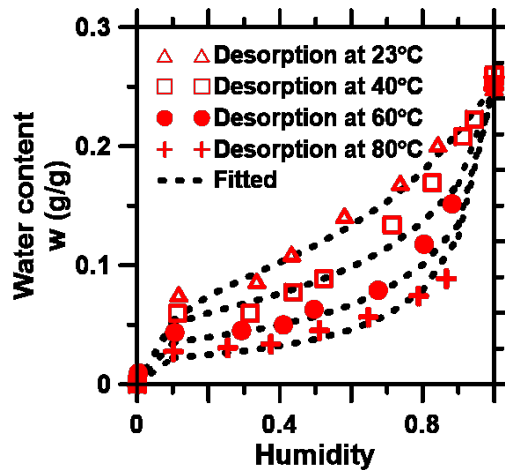


Figure 4: Influence of temperature on water vapor desorption isotherms and its comparison with experimental results for cement paste with a w/c of 0.45.

2.4 Material Models for Stage 2 Analysis

This section describes the constitutive relationships for the Stage 2 stress and damage analysis. The parameters used to describe the governing equation are presented in the form of rheological models in Figure 5. These parameters depend on the temperature and RH (obtained from Stage 1), and on neutron fluence. Neutron fluence is obtained by assuming a constant flux across the depth of the specimen.

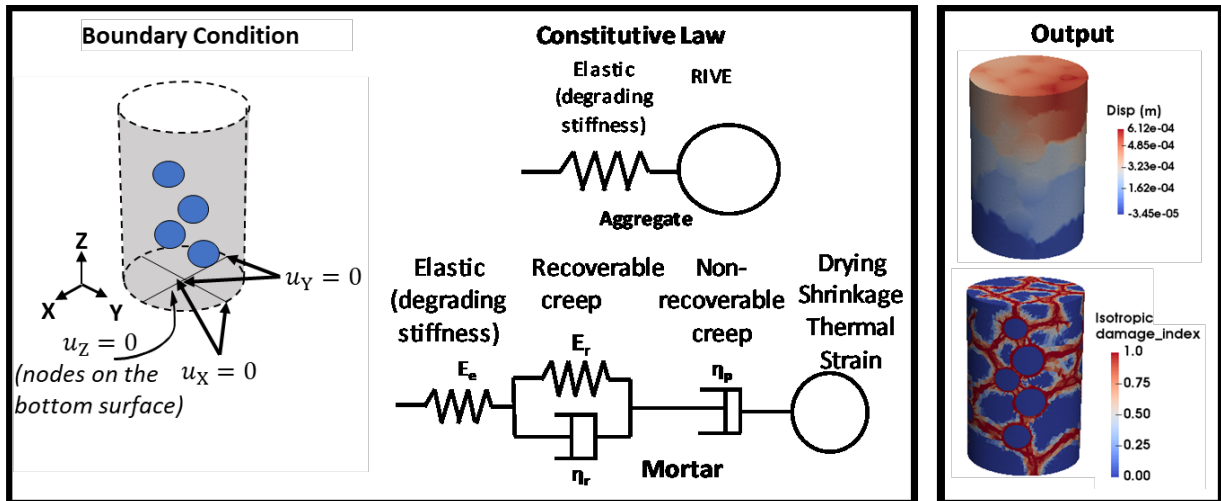


Figure 5: Schematic representation of constitutive law for mechanical analysis

2.4.1 Aggregate

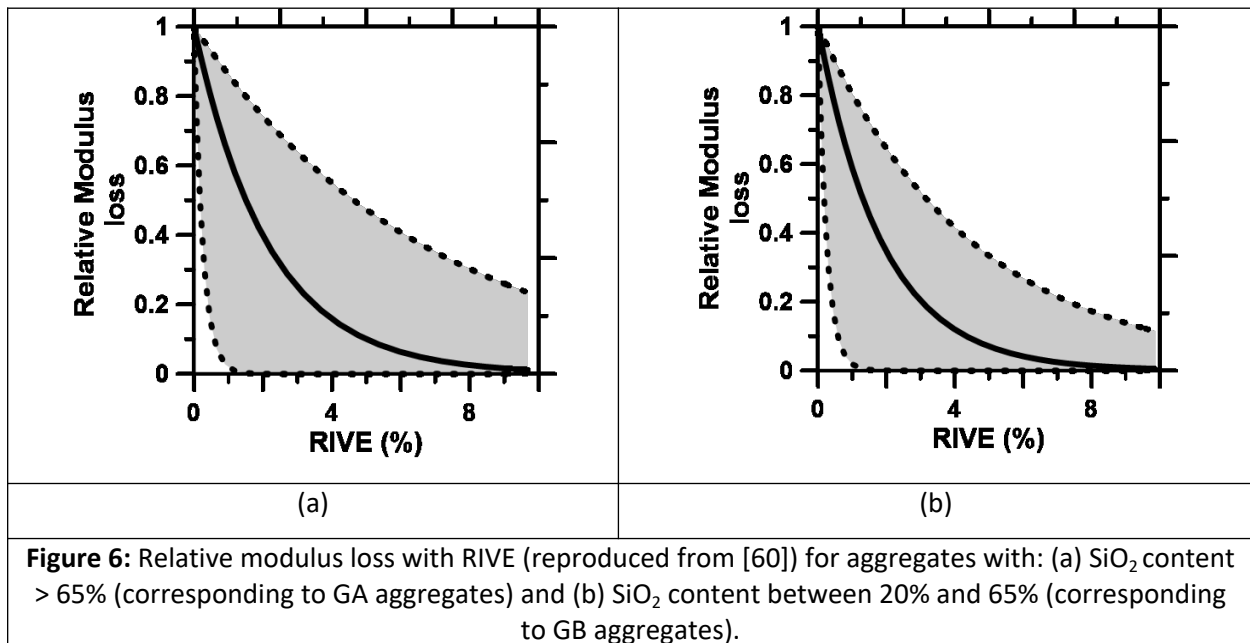
Aggregate is treated as a linear elastic material undergoing RIVE and damage (resulting in stiffness reduction) due to neutron impingement. The aggregate properties, including RIVE, are assumed to be homogeneous.

2.4.1.1 RIVE of aggregates

It is considered that RIVE of aggregates results in initiation and propagation of damage in the cement paste due to its low tensile capacity. RIVE is noted to result in significant dimensional changes, even higher than those observed for alkali-silica reaction (ASR) [3,4]. Aggregates with covalent bonds (e.g., siliceous aggregates) are more susceptible to RIVE than aggregates with ionic bonds (e.g., limestone). Quartz, which is present in aggregates, is more susceptible to amorphization and consequent volumetric change and loss of elastic properties; however, other minerals, texture, and grain boundaries also influence the rate of expansion [5]. The reduction of stiffness occurs due to the complex assemblages of different minerals in the aggregates undergoing differential shrinkage with fluence. This differential shrinkage induces lattice change, void creation, and cracking between minerals, and leads to the reduction of macroscopic Young's modulus of aggregates. In the experimental studies reported in [5], no measurements of elastic modulus loss of aggregates were carried out as a function of neutron irradiation. There are no directly available data on the loss of modulus with the increase in radiation fluence ($E > 0.1$ MeV) for these aggregates. As a result, these need to be deduced indirectly from available literature. A recent micromechanical investigation on irradiated aggregates with different SiO_2 contents found that the formation of extra voids/defects or cracks can contribute substantially to the RIVE than individual mineral expansion [60]. This study also reported that the relative loss of modulus is

more significant in aggregates with higher silica content at comparable RIVE levels, and classifies aggregates into three groups based on their silica content: high silica content: > 65%, intermediate silica content: between 20% and 65%, and low silica content: < 20%. The aggregates GA and GB belong to the high and intermediate silica content groups respectively. The loss of elastic modulus for these groups are expressed in terms of RIVE as:

where E_d and E_u are the damaged and undamaged static elastic modulus of the aggregate, ϵ_r is the radiation induced volumetric strain, and k is a factor, equal to 47.1 for GA (high silica content) and 53.1 for GB (intermediate silica content) aggregates. The relative modulus loss range as a function of RIVE is quite large as shown in Figures 6(a) and 6(b) for the two aggregate groups, because of the wide range of silica contents.



It is to be noted that temperature also affects the degree of quartz metamictization [14]. It was determined that the expansion decreases with increasing temperature, indicating that thermal heating has the capability to heal the damage in the aggregates. The thermal-healing effect is incorporated as reported in [14], and RIVE is expressed using the nucleation and growth model [4,5,61] as:

where ϵ_{max} is the maximum volumetric expansion observed in the experiments, Φ is the fast neutron fluence ($E > 0.1\text{MeV}$), Φ_{50} is the fast neutron fluence when expansion approaches half the maximum volumetric

expansion, is the temperature, and is the dimensional coefficient based on past data on amorphization of aggregates, which ranges between 2 and 5. is given as shown in Equation 18 [5].

It should be mentioned that nucleation and growth model is only suitable for individual minerals and not for polycrystalline assemblages. The use of this model for aggregate GA is justified by the fact that GA has 97% quartz, and it is assumed that only quartz expands. For aggregate GB, we have fitted this model to the experimental data available. For such polycrystalline assemblage, a micromechanical evaluation could be carried out to assess the expansion using individual grains, their expansion and overall void generation in the assemblage due to differential expansion as reported in [60].

Thermal deformation, which is expected to be negligible in comparison to RIVE, is ignored in the simulations where irradiation is considered; however, it is accounted for in the cases where only thermal heating occurs. Moreover, elevated temperature has been reported to cause healing and thus reduces the impact of RIVE [14].

2.4.1.2 Thermal expansion of aggregates

It is well known that thermal deformation is related to the applied temperature using the coefficient of thermal expansion, as:

where is the thermal strain, and and are the applied temperature and the reference temperature, respectively. This is considered for cases where only thermal heating occurs. Note that heating tests and cold tests were also carried out by Maruyama et al. [5] to isolate factors other than neutron irradiation that cause physical changes in the properties of aggregates.

2.4.2 Mortar

Mortar has been modeled as an elastic material undergoing stiffness degradation, drying shrinkage, thermal expansion and creep owing to the elevated temperature. Since the mortar consists of the cement paste and sand, the properties of mortar are homogenized based on those of the constituent phases.

2.4.2.1 Creep of mortar

There is not much data in the open literature about the effect of irradiation on the creep of concrete. Based on experiments, McDowall [62] concluded that creep is reduced under gamma irradiation while shrinkage is increased. The specimens used in the experiments that are simulated in this work were

sealed in copper foils, and radiolytic gas was allowed through a gas bubbler filled with water. Thus, limited moisture transport occurred through the venting gas, and it can be safely assumed that the creep and shrinkage kinetics are primarily due to gamma ray exposure. However in another study [63], cement paste grout specimens were exposed to neutron and gamma radiation and it was observed that creep kinetics increased by an order of magnitude compared to creep of specimens at similar temperatures, thus contradicting McDowall's [62] observations. Due to the limited and contradictory data, the effect of irradiation on creep is ignored in the present simulations. This approximation is necessitated by the fact that very little understanding exists on how irradiation affects concrete creep and shrinkage. However, the effect of humidity and temperature are considered here since creep is well known to be dependent on these parameters [20]. Burgers' model is employed to describe the constitutive behavior of mortar. Burgers' model, shown in Figure 5, consists of a spring (spring elasticity, E), a single Kelvin-Voigt chain (spring elasticity, E_1 , dashpot viscosity, η_1), and an additional dashpot (viscosity η_2). This is used to model the elastic response, the short term (recoverable) and long term (non-recoverable) creep as explained elsewhere [15]. The long term (non-recoverable) creep response of cementitious materials varies logarithmically with time, which is modeled by introducing time-dependence in the viscosity of the standalone dashpot [15,64,65].

where t_0 is a material parameter that dictates when the material enters the long-term creep region. The effect of elevated temperature on creep is considered using the Arrhenius law, such that the creep is accelerated at higher temperature. It is assumed that elevated temperature increases both the recoverable and non-recoverable creep such that the viscosities of both the dashpots are given as [20,64]:

where T_0 is the activation temperature for creep (5000 K [64]). Arrhenius law is also applied to the material parameter t_0 [15].

Creep in concrete also depends on the moisture content and it has been observed that it reduces under low RH [66]. This phenomenon is reproduced by expressing the elasticity of Kelvin-Voigt unit and non-recoverable viscosity of dashpot as [15,67]:

where α is taken as 0.2 [15]. Also, since both recoverable and non-recoverable creep has its origins in C-S-H layers, their viscosities are considered the same, and its value is taken as 40 GPa-days [15].

2.4.2.2 Thermal expansion of mortar

The thermal expansion of mortar is determined based on the applied temperature and the coefficient of thermal expansion of mortar (α_m), using an equation similar to Equation 19. α_m is usually larger than that of the aggregates, and depends on the moisture content in the pores and equilibrium RH [68,69].

2.4.2.3 RIVE of sand particles and drying shrinkage of cement paste

As concrete dries, the pore RH decreases, which causes the cement paste to shrink. The RIVE of quartz-sand particles present in the mortar is considered to limit the shrinkage of the cement paste. This approximation is necessitated by the fact that only larger aggregates are considered in the mesoscale simulations, as described earlier. Thus, the influence of RIVE of sand is adjusted in the drying shrinkage of the paste, and thus a net deformation is considered. The linear drying shrinkage of cement pastes can be directly related to the pore water content or the internal pore RH of the specimen, as shown in Equation 23 [19,70].

where α_{free} is the free shrinkage coefficient (equal to maximum shrinkage of the cement paste). Experimental results have shown that the free shrinkage coefficient is dependent upon the temperature and its value decreases at higher temperature [71]. The shrinkage is largely dependent upon the moisture content in the cement paste; however higher temperature results in smaller drying shrinkage (consequently lower free shrinkage coefficient). At lower moisture contents (< 0.08 g/g-dried paste), the shrinkage strain is dependent on the incremental loss of moisture and not the absolute moisture present as the evaporable water content is higher at lower temperature. This indicates that some part of evaporable water content does not contribute towards the shrinkage strain, resulting in a lower shrinkage strain at higher temperatures. This was also reflected in the experiments reported in [71]. This phenomenon is attributed to the microstructure reorganization at elevated temperatures. The C-S-H agglomerates likely densifies on account of elevated temperature creating larger gel pores, which does not contribute substantially to irreversible shrinkage.

The RIVE of the sand particles is calculated using Equation 17. The phase composition of sand was similar to that of the GB aggregate; hence, the properties of GB aggregate are used when computing the RIVE of sand. The net computed volumetric strain imposed on the mortar is then given as:

is the volume fraction of sand. The RIVE of sand particles can be taken to follow the pattern of that of the coarse aggregates (Equation 17), and the multiplication by 3 is to convert the linear strain into its equivalent volumetric strain component. The RIVE of sand particles might cause damage in the surrounding paste, but this has not been considered in the current simulation because of difficulties in simulating very small particles.

2.4.2.4 Stress-strain response

Mortar is treated as a quasi-brittle material. The mechanism of failure and the fracture energy are highly sensitive to the rate of application of load, temperature, and RH [72]. At lower rates of loading, creep occurs in the fracture-process zone, releasing built-up energy. This has also been shown experimentally in [73]. It can be assumed that, in the irradiation environment, the crack growth will be slower than that under mechanical loading, due to the slow expansion of aggregates. An isotropic damage model is used here because of the capability to simulate the damage response by specifying the softening function. It is widely known that softening models can result in significant mesh sensitivity in the results. The use of a softening model that is dependent on element size and fracture energy minimizes this issue. The stress in an isotropic damage model is given as [74,75]:

where, σ , ϵ , and D are the second-order stress and elastic-strain tensors, and C a fourth-order elasticity tensor, respectively. ϵ_{eq} is the state variable that captures the strain history, denoted as the equivalent strain, and D is the isotropic damage index. Damage initiates when the Rankine criterion (maximum strength greater than the tensile strength) is met, and evolves when the equivalent strain (which is a function of component of strain tensor) with increasing or remaining constant. For a one-dimensional (1D) case, the equivalent strain is equal to the maximum principal strain. For a 3D case, ϵ_{eq} is given as [75,76]:

where ν and σ_c/σ_t are the Poisson's ratio and compressive-tensile strength ratio, respectively. I_1 and I_2 are the first and second invariants of elastic strain. Once damage initiates, the stress is assumed to decay exponentially with an increase in strain (exponential softening) given as:

where ϵ_c is the equivalent strain at which cracking begins. The parameter β controls the exponential softening slope and depends on the fracture energy as:

where l_c is the characteristic length associated with each element and depends on the element type and its size. This formulation ensures that for a given localized crack, fracture energy released is independent of the mesh size, and avoids vanishing energy dissipation as the mesh size is reduced.

2.5 Boundary Conditions

Finite element models with boundary conditions for both the stages of simulation were shown in Figure 3 and Figure 5. For Stage 1, convective boundary conditions were applied on the sides for the exchange of heat with the surroundings while Dirichlet boundary conditions were assumed for the mortar for exchange of moisture with the surroundings. These conditions are given as:

where k is the thermal conductivity of the aggregate or mortar, h is the heat transfer coefficient, and T_s and T_a are the surface and ambient temperatures, and ϕ_s and ϕ_a are the surface and ambient humidities respectively. It is assumed that no exchange of heat and moisture takes place from the top and bottom of the specimen. In the actual experiment, nine specimens were stacked one over the other, in the capsule. Hence, moisture or heat loss could occur only from the sides of the specimen.

For Stage 2, all the nodes on the bottom surface are fixed in the Z direction. Two nodes on the X and Y axes are fixed in the Y-direction and X-direction, respectively. This constrains the specimen against motion in all the six rigid body models. The change in length is measured by measuring the displacement of the nodes on the top surface.

3 FINITE ELEMENT IMPLEMENTATION AND SIMULATION RESULTS

The Agave high-performance computing cluster at Arizona State University was employed to carry out the simulations using a single node with 28 cores and 128 GB RAM. It took approximately 1 hour and 48 hours wall clock time, respectively, to complete Stage 1 and 2 analyses. An algorithm, based on the formulation described above was implemented based on the MOOSE framework, an open-source object

oriented finite element analysis toolkit developed by the Idaho National Laboratory (INL) [33] that solves large coupled systems of equations simultaneously [33,34]. MOOSE can utilize several approaches, including the Jacobian free Newton Krylov (JFNK) technique to solve these equation systems. MOOSE has a modular architecture that allows for additional physics models to be readily implemented using multiple types of pluggable modules for various portions of the model. For example, the modules called kernels in MOOSE represent the individual terms of the weak form of the governing partial differential equation. Boundary conditions are terms in the weak form that act on boundaries. Material objects represent the different material behavior (elasticity, plasticity, cracking) and are used to store the material properties (elastic modulus, humidity, diffusivity etc.) that can be used by kernels, boundary conditions, and material objects, themselves. This pluggable object-oriented system allows code reusability and enables easier addition of new capabilities. This framework lends itself well to solving the coupled physics models involved in concrete degradation. More details of MOOSE can be found in [33–35].

The current formulation uses a one-step finite-difference scheme to estimate the viscoelastic effects along with linear isotropic damage based on fracture energy to simulate the effect of cracking. In this implementation, the inelastic strain is computed first, using the creep model described above. The effective stress based on the net elastic strain is computed next. The effect of damage is then considered using the computed damage index as shown in Equation 25. The numerical implementation of the creep models are explained in detail in [77] while the damage algorithm can be found in [75]. The implementation of the coupled temperature and humidity model is described in [78]. The input parameters are described next followed by the simulations results.

3.1 Input Parameters

3.1.1 Aggregates

The dynamic moduli of aggregates GA and GB used in CON-A and CON-B, respectively, in the experiments are given as 65 and 81 GPa respectively [5]. GA is altered tuff crush aggregate while GB is felsic sandstone gravel (Table 9 of [5]). According to the information presented in [5], C-G4 is an altered tuff aggregate and C-G5 is a felsic sandstone. C-G5 is equivalent to aggregate GD in the experiments [5], but it has a similar phase composition as aggregate GB, as noted from Table 12 of [5], and hence an elastic modulus of 81 GPa, reported in [5] is used. Similarly, CG-4, which is similar to aggregate GA, has a modulus of 65 GPa. The static modulus is observed to be lower than the dynamic modulus by about 10% [5]. Thus, in the simulations, the dynamic modulus values are reduced by 10% to estimate the static modulus values (58.5 and 72.9 GPa, respectively). Poisson's ratio is estimated from dynamic

measurements (Figure 100 in [5]); values of 0.28 and 0.25 are used respectively for the GA and GB aggregates. The degradation of modulus with neutron fluence is determined in accordance with Equation 16 and Equation 17 and shown in Figure 7(a). Equation 16 was developed by normalizing the data provided by Denisov et al. [25] for an energy threshold 10 keV; hence the fluence was normalized to 0.1 MeV using a factor of 1.6, (the ratio of fluence at an energy of 10 keV to that of 0.1 MeV in JEEP-II reactor) when computing the Young's modulus reduction with neutron fluence as shown in Figure 7(a). The coefficient of thermal expansion is related to the amount of quartz in the material [5] (GA and GB has 92 and 47% quartz respectively) using the following equation [5]:

where α is the amount of quartz (in %) in the aggregate, and β is the coefficient of thermal expansion ($\mu/\text{°C}$). Values of $9.5 \mu\text{m/m/°C}$ and $6.9 \mu\text{m/m/°C}$ are obtained as the thermal expansion coefficients for aggregates GA and GB. For estimating RIVE, the maximum volumetric expansion is taken as 0.18 and 0.13 for GA and GB aggregates respectively, as reported in [5]. The dimensional coefficient d' is taken as 2.38 based on data provided in [4].

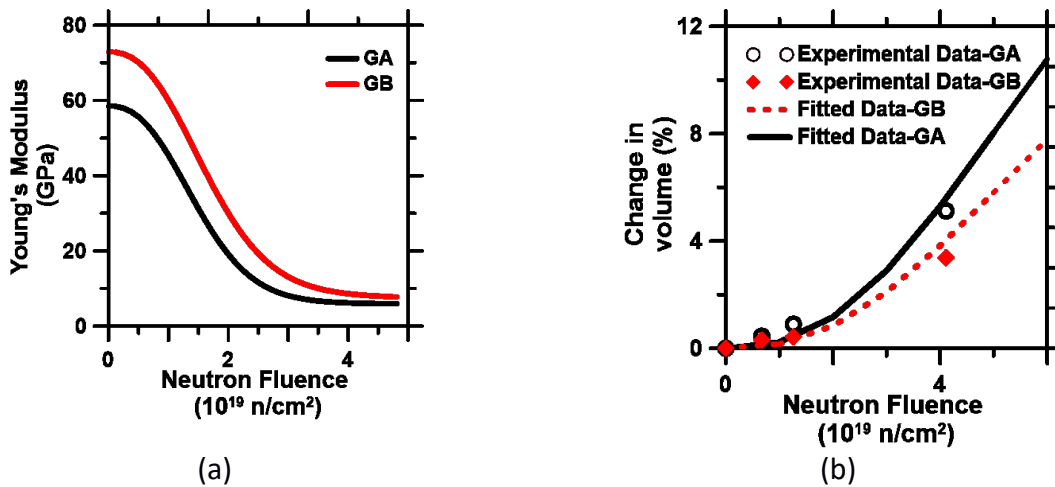


Figure 7: Variation of (a) Young's modulus, and (b) RIVE as a function of neutron fluence, for GA and GB aggregates.

3.1.2 Mortar

Mortar undergoes drying shrinkage and creep owing to the high temperature ($T \sim 70^\circ\text{C}$) and RIVE due to the presence of quartz sand in the mortar. The Poisson's ratio of the mortar is taken as 0.20. The Young's modulus of the mortar is influenced by temperature and RH. It has been shown that the modulus of high early-strength cementitious paste mixture is fairly constant at temperatures up to 90°C [79]. The modulus of mortar was back-calculated to be 24 GPa based on a self-consistent

homogenization scheme [80]. The thermal expansion coefficient of mortar was calculated by upscaling the thermal expansion coefficient of cement paste using Levin's theorem for a two-phase composite which is given as:

, and are the bulk modulus of paste, sand and concrete, and and are the thermal expansion coefficients of paste ($20 \times 10^{-6}/^\circ\text{C}$ [81] for fully saturated condition) and sand ($6.95 \times 10^{-6}/^\circ\text{C}$, which is similar to that of aggregate GB [5]). The coefficient of thermal expansion of the mortar (in saturated state) is determined as $12.2 \times 10^{-6}/^\circ\text{C}$. The variation in thermal expansion coefficient of paste with relative humidity (RH) is given in [69], and represented in Figure 8.

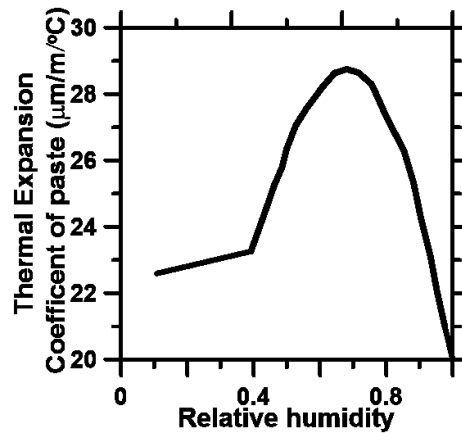


Figure 8: Variation of thermal expansion coefficient of the paste with the temperature based on [69].

2.4.2.3 RIVE of sand particles and drying shrinkage of cement paste

The tensile strength of the mortar essentially remains constant if the mortar (or concrete) is subjected to long-term heating at temperatures between 40 and 90°C [5,79]. At 70°C, which is the temperature of the irradiated concrete, the tensile strength of mortar is taken as 5 MPa [82], which is par for the type of mortar based on the cement content and w/c. In the experiments that formed the basis for the simulations, the specimens were cured for one year at 40% RH, and then treated at elevated temperatures for 3 months. The numerical simulations on irradiated concrete shows that the humidity reaches 60% inside the specimen and the temperature is 60-70°C. It should be noted that the strength of the cement paste specimens increases during radiation as observed indirectly by the increased Vickers' hardness value [5]. It is not clear at this stage how irradiation influences the tensile strength of mortar; hence variable tensile strengths are not considered. The fracture energy also is dependent on temperature. However, no such measurements are reported. As a result, the fracture

energy was calibrated based on the observed damage and expansion value of the mortar to be approximately 100 N-m/m². This is in the range of fracture energy obtained for normal strength mortars at temperature around 70-100°C [83,84]. The material properties and their values used in the finite element simulations are shown in Table 2.

Table 2: Input parameters used in the simulations. The reasons for the use parameters are explained in the appropriate sections. The multiple values reported for aggregates are for GA and GB.

<i>Variable</i>	<i>Value</i>	<i>Units</i>	<i>Variable</i>	<i>Value</i>	<i>Units</i>
Aggregates			Mortar		
	9.5, 6.9	μm/m/°C		12.2	μm/m/°C
	0.38	--		0.9	J/kg/°C
	1100	J/kg/°C		1100	J/kg/°C
	2.38	--		-4000	μm/m
	0.18, 0.13	--		24	GPa
	58.5, 72.9	GPa		5	MPa
	3	W/m/°C		100	N-m/m ²
	0.28, 0.25	--		0.2	--
	2600	kg/m ³		3	W/m/°C
Concrete				0.2	--
	6.9	μm/m/°C		40	GPa-days
	200	W/m ² /°C		40	GPa-days
	211	kJ/m ³ /s		2231	kg/m ³
	50	°C		2	days
	20	°C		5000	K
	0.4	--		50	°C
	14	--		0.5	--

3.2 Numerical Simulation Results

3.2.1 Stage 1 Analysis

A coupled hygro-thermal analysis was carried out in Stage 1 to compute the variation of temperature and pore RH inside the specimen due to irradiation, based on the material models discussed in Section 2.3. In the JEEP II experiments, nine concrete specimens (of which one was a dummy specimen to measure temperature) were irradiated together inside a double-walled aluminum capsule with coolant

water flowing in the annulus to reduce the temperature. The temperature was measured at the center of the top specimen. Moreover, the gas released by radiolysis of the pore solution was passed into a water-vapor condensation system and a gas collection branch. The generated gas was released once the pressure in the capsule exceeded 1.25 bar through a release valve. A helium gas flush line was also installed for adverse situations to flush out any condensation that might obstruct smooth discharge of gases. It was difficult to characterize the boundary conditions in this case because it would have required modeling of all specimens within the capsule, along with the flowing coolant water and a pressure release system once the pressure reached 1.25 bar. Instead of carrying out such a complex analysis, some simplifying assumptions were made. The heat transfer coefficient in Equation 29 was calibrated (shown in Table 2) so that the simulations match the temperature at the center of the specimen. It has been reported that the temperature at the center of the specimens reached 72°C quickly in the experiments, but it is not known how quickly. The experiments were designed to keep the irradiation temperature at approximately 70°C [5]. In the simulations, this temperature was reached in 16 hours and remained constant thereafter. Figure 9 shows the temperature profile in the specimen after 16 hours. The thermal properties required for Stage 1 analysis (see Section 2.3.1) for aggregates GA and GB are similar, and hence these simulations can be used for both Con-A and Con-B.

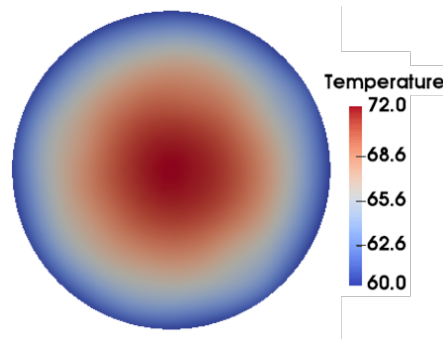


Figure 9: Plan view of the specimen temperature at 16 hours, after which it achieves a steady state condition.

As the irradiation proceeded, the moisture released by the specimen continuously decreased. No appreciable loss of moisture was reported after 100 days of irradiation. The pressure was released more frequently in the beginning due to higher available moisture in the specimen and, consequently, higher vapor release was noted early on. Thus, the capsule was always under high pressure during the radiation. The actual conditions were quite different in the reactor; however, in the simulations, a simplification was made such that the environmental humidity (in Equation 30) was calibrated to drop

exponentially at a rate such that the total water released by the specimen matched those in the experiments. It is assumed that gases and water vapor diffuse in a similar manner, and no effort is made to differentiate between the two due to the lack of understanding of diffusion under irradiation conditions. Figure 10(a) shows the assumed environmental-humidity profile while Figure 10(b) shows the experimental and simulated amounts of water released. The experimental water released consists of the water from gas that was released, and the water absorbed on the condenser for the PPT-D specimen. Note that only PPT-D or E data could be considered here because they were the specimens tested for more than 100 days. Two-thirds of the gas is assumed to consist of hydrogen. It is converted to the molar mass of water assuming STP condition (1 mole of $H_2 = 22.4 \text{ L} = 2 \text{ g}$; 1 mole of water = 18 g).

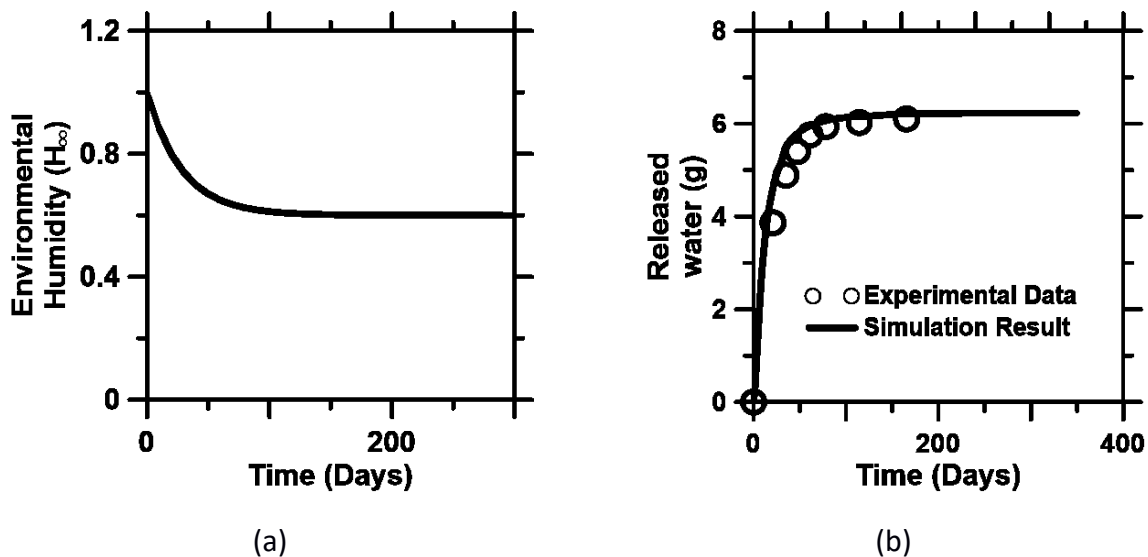


Figure 10: (a) Applied humidity at the specimen boundary, and (b) experimental and simulated amounts of water released after specified irradiation times. The simulated results correspond to the assumed applied environmental humidity at each of those times.

Figure 11 shows RH as a function of depth into the specimen and irradiation time. Currently, there is no way to validate the simulated pore humidity values as no measurements of internal RH or water content were made during the irradiation experiment. The results show that the assumption of constant humidity profile made in a previous study for irradiated concrete [15] could be used for small-diameter specimens. Note that in Figure 11, the aggregates have been removed since they do not partake in moisture transport.

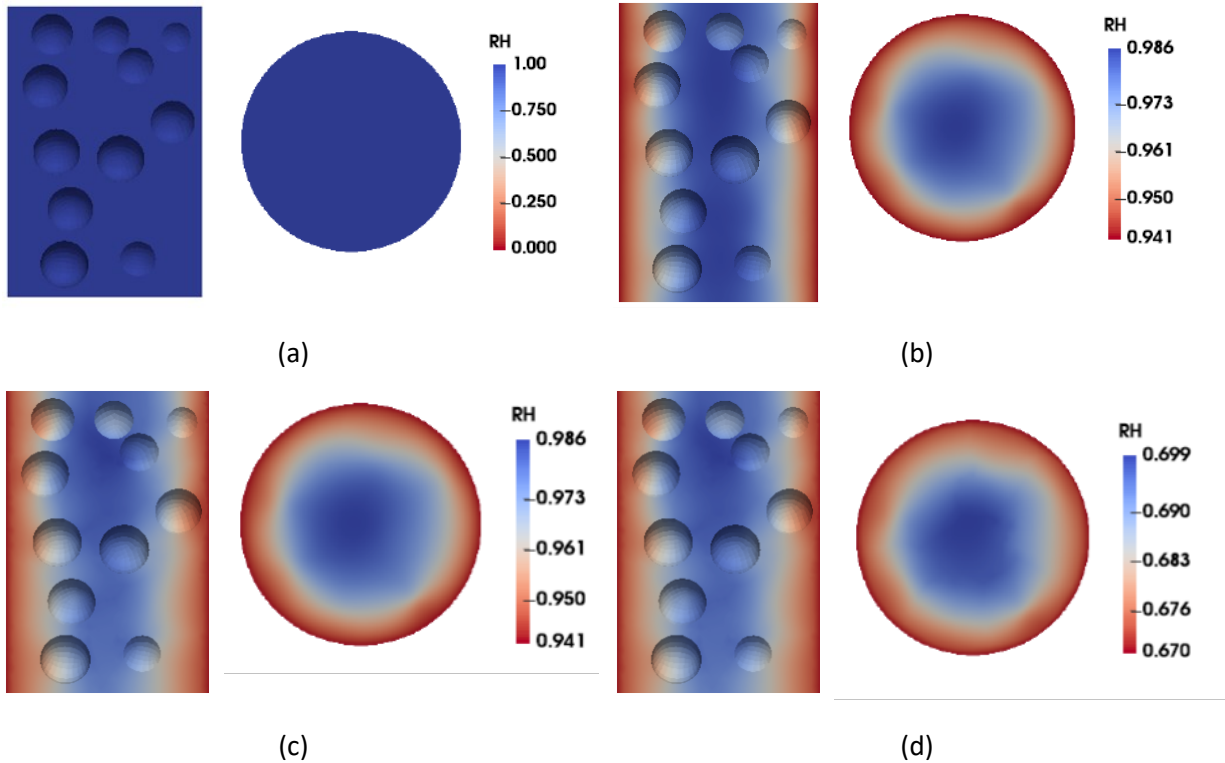


Figure 11: Evolution of RH in the specimen at: (a) 0, (b) 5, (c) 50, and (d) 100 days of irradiation. The aggregates have been removed as they do not partake in moisture transport. Please also note that the color schemes are different for all four figures; for e.g., deep red in (b) corresponds to a RH of 94%, while the same color in (d) indicates an RH of 67%. Maintaining uniformity in color schemes across all figures would have adversely impacted visual readability.

3.2.2 Stage 2 Analysis

After the temperature and humidity profiles were determined as shown above, mechanical analysis was carried out. The radiation dosage is considered constant along the depth of the specimen as it does not change appreciably over a single specimen [5]. The dosage changes appreciably over the nine specimens which underwent irradiation; however, to reduce computational complexities, only one specimen is simulated, and the average radiation rate of 3.6×10^{12} n/cm²/s is applied. The average radiation rate multiplied by time gives the total radiation dose received by the specimen at each time step. The time- and space-dependent variation of temperature and RH, along with their influence on RIVE and thermal expansion of aggregates and mortar, and shrinkage, creep, and damage development in mortar (based on the material models defined in Section 2.4) are used to simulate the length change and effective elastic modulus in the concrete subjected to irradiation for different times. The length change is computed based on the average displacement of the nodes on the top surface of the specimen and is

compared to the experimental values of CON-A and CON-B, in Figure 12(a). The simulations are observed to capture the length change of the irradiated concrete adequately.

The damage in the mortars of CON-A and CON-B, represented by the isotropic damage index (Section 2.4.2.4), volume-averaged over all the finite elements in the mortar, are shown in Figure 12(b). Note that the damage in the mortar is mainly because of the RIVE of aggregates. The damage index is higher for the mortar in CON-A, especially after 45 days or so when simulations show extensive damage (see Figure 13). The onset of damage is slightly delayed for CON-B because of the lower volume change of aggregate GB as shown in Figure 7(b), attributable to its reduced quartz content (as seen in Figure 12(b)). The progression of damage in the CON-A and CON-B specimens, up to an irradiation time of 150 days, are shown in Figures 13(a) and (b). Damage initiates, propagates around the aggregates, and then bridges the aggregates. Cracking was observed to have initiated in the CON-A specimen at the end of 36 days, and at the end of 38 days for the CON-B specimen. At the end of 40, 48, 72, and 150 days, there was slightly more damage in CON-A, mainly because of higher RIVE in aggregate GA.

In the experimental measurements, the specimens were heated at 76°C before carrying out the length change and elastic modulus measurements. In the simulations, the specimens were heated at 76°C at the end of 30 days (PPT-B), 50 days (PPT-C) and 155 days (PPT-D) tests, and it was observed that the length and elastic modulus changes due to heating of the specimen were insignificant. Thus, RIVE is the driving force behind the length change and modulus degradation.

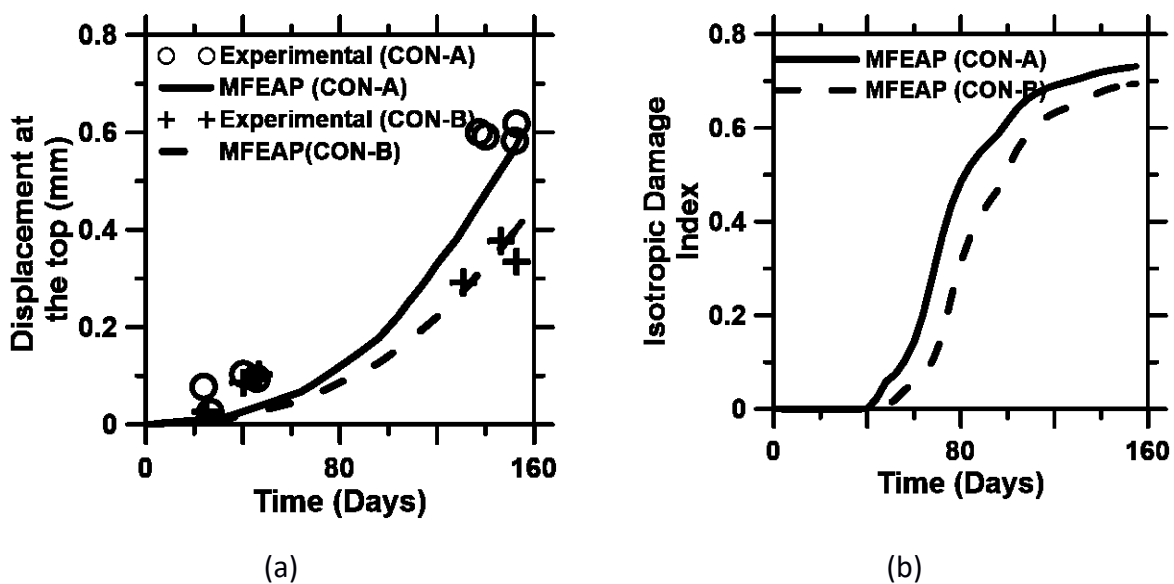


Figure 12: MOOSE finite element analysis predictions (MFEAP) for: (a) displacement at the top of the

specimen, and (b) damage index in the mortars, as a function of irradiation time for CON-A and CON-B. The displacement at the top is compared directly with the experimental results, while the isotropic damage index is used to compute the elastic modulus degradation of the specimens as shown in

Figure 14.

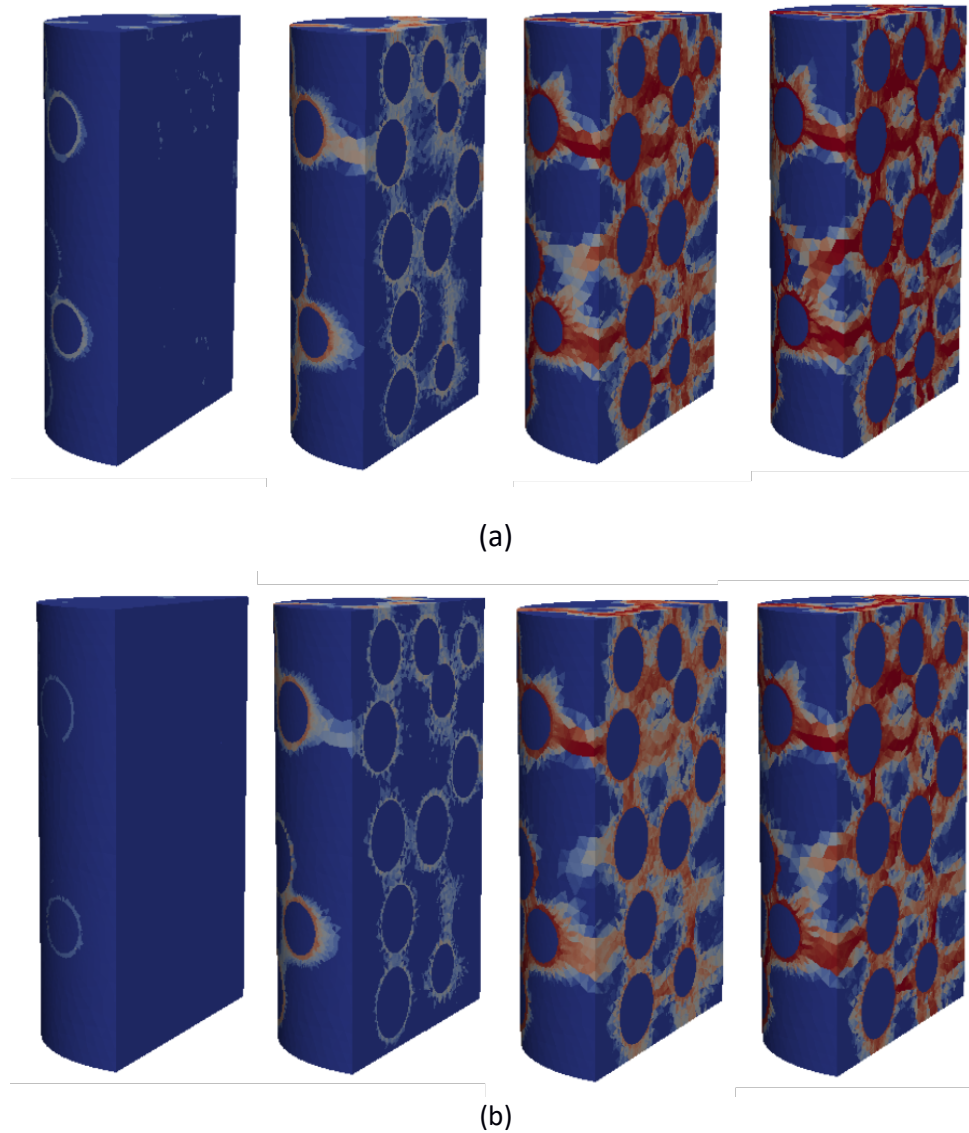


Figure 13: Progression of damage in: (a) CON-A, and (b) CON-B specimens at the at the end of 40, 48, 72, and 150 days of irradiation.

As shown in Figure 7(a), the elastic modulus of the aggregates degrades with fluence (or irradiation time). The irradiation time-dependent elastic modulus of the mortar, as a function of the volume-

averaged damage (obtained from the simulations (see Section 2.4.2.4) is computed as follows:

The Young’s modulus of CON-A and CON-B after different times of irradiation are then computed based on a self-consistent scheme [80], shown in Figure 14 (bold line) using the damaged modulus of aggregate and mortar. The radiation-affected aggregate modulus was obtained from Figure 7(a) and mortar modulus from Equation 33. Due to the large variation in the modulus values of the irradiation-damaged aggregates as evident from Figure 6(a), simulations were also carried out using the lower and upper bounds of the aggregate moduli. The corresponding predictions are also plotted in Figure 14 (as dotted lines). In general, the experimentally determined elastic moduli after different durations of irradiation fall within the bounds shown. This indicates that radiation induced aggregate stiffness loss plays an important part in the loss of mechanical properties, and this should be determined as accurately as possible. Predictions using other micromechanical models, e.g., Hansen [85], Counto [86], and Eshelby’s method [87,88] also were found to lie within or very close to the these bounds. The elastic modulus of CON-A and CON-B drops from 36 GPa to 7 GPa and 37 GPa to 9.12 GPa respectively during the 155 days of irradiation. The two-stage modeling scheme that considers the multi-physics mechanisms at play during irradiation is shown to successfully predict the degradation in elastic modulus of irradiated concrete specimens.

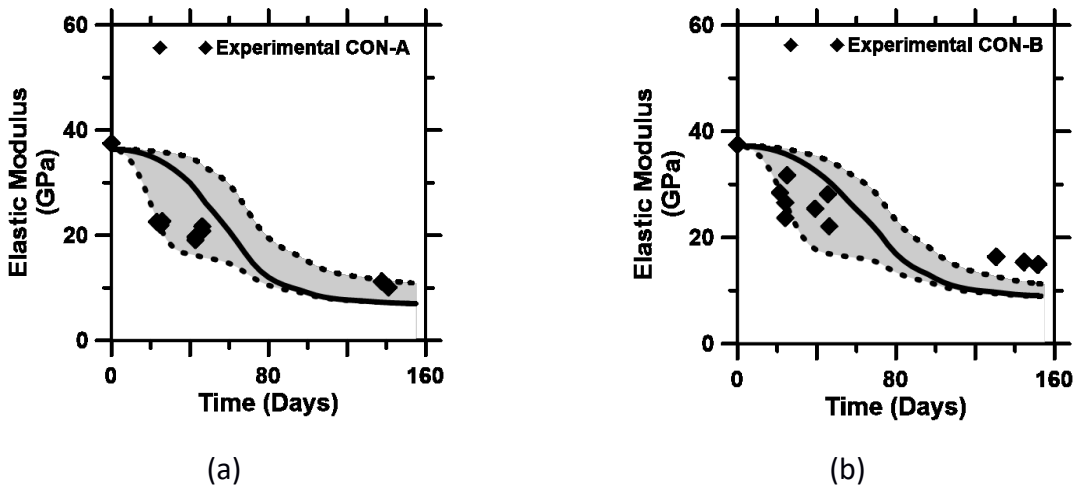


Figure 14: Comparison of elastic modulus as a function of irradiation time for: (a) CON-A and (b) CON-B specimens. The bold lines represent the drop in concrete modulus when irradiated, obtained using the best fit curve of aggregate modulus drop with RIVE shown in Figure 6. The dotted lines indicate the upper-and-lower bounds of concrete modulus by using the bands shown in Figure 6.

4 SUMMARY AND CONCLUSIONS

This paper presents a comprehensive 3D mesoscale finite element framework to model the damage in concrete under neutron irradiation in a test reactor using two-stage simulations. The framework considers the effects of neutron irradiation, secondary gamma irradiation, and high temperature on the mortar and aggregates separately. Modeling is carried out using the MOOSE framework to simulate RIVE and radiation induced damage of coarse aggregates and the corresponding damage propagation in the mortar undergoing creep, thermal strains, and drying shrinkage. A comprehensive experimental data set [5] was used to aid simulations reported in this paper. The parameters for the simulation were either directly available from the experiments or were assumed with theoretical justifications.

The multi-physics simulation reported in this paper was performed in two stages. In the first stage, the temperature and humidity profiles in the specimen as a result of incident radiation energy were computed using a coupled hygro-thermal model. The thermal-transport modeling was based on energy and mass balance in a capillary porous solid and considered the effects of all the constituents of concrete, including the free water. Moisture-transport characteristics were accounted for using empirical sorption-desorption isotherms. The temperature and humidity profiles computed from this stage, along with the irradiation dose, formed the inputs to the second stage of analysis to predict the mechanical properties under irradiation.

Aggregate properties, including RIVE, were assumed to be homogeneous in the second-stage analysis. The RIVE of coarse aggregates was computed using a nucleation-and-growth model fitted to the experimental data. The irradiation-induced elastic modulus degradation of aggregates followed the results of a micromechanical investigation on irradiated aggregates, that accounted for the silica content in the aggregates. While fine aggregates are also subjected to RIVE, it was assumed that, in the mortar, the shrinkage of the paste at high temperature counteracted this expansion. This assumption was required by the fact that only coarse aggregates were considered in the mesoscale simulations. The damage in the mortar was quantified using exponential softening and an isotropic damage parameter, which in turn was used to determine the elastic modulus of mortar as a function of irradiation time. The effective elastic modulus of concretes containing two different coarse-aggregate types as a function of irradiation time was determined using the self-consistent scheme. The experimental values of the elastic modulus and expansion of concretes after irradiation in the test reactor were found to match well with the predictions. Simulations demonstrated that RIVE of aggregates initially causes cracks around the aggregates, that, with further irradiation, propagate to damage the mortar. The proposed framework

provides a numerical tool to predict damage in concrete under irradiation, considering all attendant mechanisms.

5 ACKNOWLEDGMENTS

NS, GB, SR, GS, and NN sincerely acknowledge the financial support for this research from the Department of Energy's Nuclear Energy University Program (DOE-NEUP: DE-NE0008398). This manuscript has been co-authored by UT-Battelle, LLC (DE-AC05-00OR22725) (AG) and Battelle Energy Alliance, LLC (DE-AC07-05ID14517) (BS) under contract with the U.S. Department of Energy. The contents of this paper reflect the views and opinions of the authors, who are responsible for the accuracy of data presented, and do not necessarily reflect the views and policies of the funding agency, nor do the contents constitute a standard, specification, or regulation. The U.S Government retains and the publisher, by accepting the article for publication, acknowledges that the United States Government retains a nonexclusive, paid-up, irrevocable, world-wide license to publish or reproduce the published form of this manuscript, or allow others to do so, for United States Government purposes.

6 REFERENCES

- [1] www.energy.gov, What's the Lifespan for a Nuclear Reactor? Much Longer Than You Might Think, Energy.Gov. <https://www.energy.gov/ne/articles/whats-lifespan-nuclear-reactor-much-longer-you-might-think> (accessed March 24, 2020).
- [2] nrc.gov nrc.gov, NRC: Backgrounder on Reactor License Renewal. <https://www.nrc.gov/reading-rm/doc-collections/fact-sheets/fs-reactor-license-renewal.html#status> (accessed March 19, 2020).
- [3] B. Pomaro, A Review on Radiation Damage in Concrete for Nuclear Facilities: From Experiments to Modeling, *Model. Simul. Eng.* (2016). <https://doi.org/10.1155/2016/4165746>.
- [4] K.G. Field, I. Remec, Y.L. Pape, Radiation effects in concrete for nuclear power plants – Part I: Quantification of radiation exposure and radiation effects, *Nucl. Eng. Des.* 282 (2015) 126–143. <https://doi.org/10.1016/j.nucengdes.2014.10.003>.
- [5] I. Maruyama, O. Kontani, M. Takizawa, S. Sawada, S. Ishikawao, J. Yasukouchi, O. Sato, J. Etoh, T. Igari, Development of Soundness Assessment Procedure for Concrete Members Affected by Neutron and Gamma-Ray Irradiation, *J. Adv. Concr. Technol.* 15 (2017) 440–523. <https://doi.org/10.3151/jact.15.440>.
- [6] L.F. Elleuch, F. Dubois, J. Rappeneau, Effects of Neutron Radiation on Special Concretes and Their Components, *Spec. Publ.* 34 (1972) 1071–1108. <https://doi.org/10.14359/18107>.
- [7] M. Wittels, F.A. Sherrill, Radiation Damage in SiO₂ Structures, *Phys. Rev.* 93 (1954) 1117–1118. <https://doi.org/10.1103/PhysRev.93.1117.2>.
- [8] L.W. Hobbs, M.R. Pascucci, Radiolysis and defect structure in electron-irradiated α -quartz, *J. Phys. Colloq.* 41 (1980) C6-237-C6-242. <https://doi.org/10.1051/jphyscol:1980660>.
- [9] J.P. Bonnet, M. Boissier, A. Ait Gherbi, The amorphization process of neutron-irradiated crystalline quartz studied by Brillouin scattering, *J. Non-Cryst. Solids.* 167 (1994) 199–204. [https://doi.org/10.1016/0022-3093\(94\)90385-9](https://doi.org/10.1016/0022-3093(94)90385-9).
- [10] L. Douillard, J.P. Duraud, Amorphization of α -Quartz under Irradiation, *J. Phys. III.* 6 (1996) 1677–1687. <https://doi.org/10.1051/jp3:1996206>.
- [11] R.C. Ewing, A. Meldrum, L. Wang, S. Wang, Radiation-induced amorphization, *Rev. Mineral. Geochem.* 39 (2000) 319–361. <https://doi.org/10.2138/rmg.2000.39.12>.
- [12] B. Wang, N.M.A. Krishnan, Y. Yu, M. Wang, Y. Le Pape, G. Sant, M. Bauchy, Irradiation-induced topological transition in SiO₂: Structural signature of networks' rigidity, *J. Non-Cryst. Solids.* 463 (2017) 25–30. <https://doi.org/10.1016/j.jnoncrsol.2017.02.017>.

- [13] B. Wang, Y. Yu, I. Pignatelli, G. Sant, M. Bauchy, Nature of radiation-induced defects in quartz, *J. Chem. Phys.* 143 (2015) 024505. <https://doi.org/10.1063/1.4926527>.
- [14] V.N. Bykov, A.V. Denisov, V.B. Dubrovskii, V.V. Korenevskii, G.K. Krivokoneva, L.P. Muzalevskii, Effect of irradiation temperature on the radiation expansion of quartz, *Sov. At. Energy.* 51 (1981) 593–595.
- [15] A. Giorla, M. Vaitová, Y. Le Pape, P. Štemberk, Meso-scale modeling of irradiated concrete in test reactor, *Nucl. Eng. Des.* 295 (2015) 59–73. <https://doi.org/10.1016/j.nucengdes.2015.08.027>.
- [16] Y.-H. Hsiao, B. Wang, E.C. La Plante, I. Pignatelli, N.M.A. Krishnan, Y. Le Pape, N. Neithalath, M. Bauchy, G. Sant, The effect of irradiation on the atomic structure and chemical durability of calcite and dolomite, *Npj Mater. Degrad.* 3 (2019) 36. <https://doi.org/10.1038/s41529-019-0098-x>.
- [17] S. Ishikawa, I. Maruyama, M. Takizawa, J. Etoh, O. Kontani, S. Sawada, Hydrogen Production and the Stability of Hardened Cement Paste under Gamma Irradiation, *J. Adv. Concr. Technol.* 17 (2019) 673–685. <https://doi.org/10.3151/jact.17.673>.
- [18] I. Maruyama, S. Ishikawa, J. Yasukouchi, S. Sawada, R. Kurihara, M. Takizawa, O. Kontani, Impact of gamma-ray irradiation on hardened white Portland cement pastes exposed to atmosphere, *Cement and Concrete Research.* 108 (2018) 59–71. <https://doi.org/10.1016/j.cemconres.2018.03.005>.
- [19] Z.P. Bažant, *Mathematical Modeling of Creep and Shrinkage of Concrete*, John Wiley Sons Inc N. Y. N.
- [20] Z.P. Bažant, Mathematical model for creep and thermal shrinkage of concrete at high temperature, *Nucl. Eng. Des.* 76 (1983) 183–191. [https://doi.org/10.1016/0029-5493\(83\)90133-4](https://doi.org/10.1016/0029-5493(83)90133-4).
- [21] Y. Wang, Y. Xi, The Effect of Temperature on Moisture Transport in Concrete, *Materials.* 10 (2017) 926. <https://doi.org/10.3390/ma10080926>.
- [22] B. Pomaro, V.A. Salomoni, F. Gramegna, G. Prete, C.E. Majorana, Radiation damage evaluation on concrete within a facility for Selective Production of Exotic Species (SPES Project), Italy, *J. Hazard. Mater.* 194 (2011) 169–177. <https://doi.org/10.1016/j.jhazmat.2011.07.079>.
- [23] B. Pomaro, V.A. Salomoni, F. Gramegna, G. Prete, C.E. Majorana, Radiation damage evaluation on concrete shielding for nuclear physics experiments, *Ann. Solid Struct. Mech.* 2 (2011) 123–142. <https://doi.org/10.1007/s12356-011-0023-7>.
- [24] V.A. Salomoni, C.E. Majorana, B. Pomaro, G. Xotta, F. Gramegna, Macroscale and

- mesoscale analysis of concrete as a multiphase material for biological shields against nuclear radiation, *Int. J. Numer. Anal. Methods Geomech.* 38 (2014) 518–535. <https://doi.org/10.1002/nag.2222>.
- [25] A.V. Denisov, V.B. Dubrovsky, V.N. Solovyov, Radiation Resistance of Mineral and Polymer Construction Materials, ZAO MEI 691 Publishing House. In Russian, 319.
- [26] Y. Le Pape, M.H.F. Alsaïd, A.B. Giorla, Rock-Forming Minerals Radiation-Induced Volumetric Expansion – Revisiting Literature Data, *J. Adv. Concr. Technol.* 16 (2018) 191–209. <https://doi.org/10.3151/jact.16.191>.
- [27] Y. Xi, Z.P. Bažant, H.M. Jennings, Moisture diffusion in cementitious materials Adsorption isotherms, *Adv. Cem. Based Mater.* 1 (1994) 248–257. [https://doi.org/10.1016/1065-7355\(94\)90033-7](https://doi.org/10.1016/1065-7355(94)90033-7).
- [28] Y. Xi, Z.P. Bažant, L. Molina, H.M. Jennings, Moisture diffusion in cementitious materials Moisture capacity and diffusivity, *Adv. Cem. Based Mater.* 1 (1994) 258–266. [https://doi.org/10.1016/1065-7355\(94\)90034-5](https://doi.org/10.1016/1065-7355(94)90034-5).
- [29] H. Gross, High-temperature creep of concrete, *Nucl. Eng. Des.* 32 (1975) 129–147. [https://doi.org/10.1016/0029-5493\(75\)90095-3](https://doi.org/10.1016/0029-5493(75)90095-3).
- [30] Y. Le Pape, K.G. Field, I. Remec, Radiation effects in concrete for nuclear power plants, Part II: Perspective from micromechanical modeling, *Nucl. Eng. Des.* 282 (2015) 144–157. <https://doi.org/10.1016/j.nucengdes.2014.10.014>.
- [31] Y. Jing, Y. Xi, Long-term neutron radiation levels in distressed concrete biological shielding walls, *J. Hazard. Mater.* 363 (2019) 376–384. <https://doi.org/10.1016/j.jhazmat.2018.09.080>.
- [32] I. Maruyama, K. Haba, O. Sato, S. Ishikawa, O. Kontani, M. Takizawa, A Numerical Model for Concrete Strength Change under Neutron and Gamma-ray Irradiation, *J. Adv. Concr. Technol.* 14 (2016) 144–162. <https://doi.org/10.3151/jact.14.144>.
- [33] C.J. Permann, D.R. Gaston, D. Andrs, R.W. Carlsen, F. Kong, A.D. Lindsay, J.M. Miller, J.W. Peterson, A.E. Slaughter, R.H. Stogner, R.C. Martineau, MOOSE: Enabling Massively Parallel Multiphysics Simulation, *ArXiv191104488 Phys.* (2019). <http://arxiv.org/abs/1911.04488> (accessed November 16, 2019).
- [34] D. Gaston, C. Newman, G. Hansen, D. Lebrun-Grandié, MOOSE: A parallel computational framework for coupled systems of nonlinear equations, *Nucl. Eng. Des.* 239 (2009) 1768–1778. <https://doi.org/10.1016/j.nucengdes.2009.05.021>.

- [35] A.E. Slaughter, J.W. Peterson, D.R. Gaston, C.J. Permann, D. Andrš, J.M. Miller, Continuous Integration for Concurrent MOOSE Framework and Application Development on GitHub, *J. Open Res. Softw.* 3 (2015) e14. <https://doi.org/10.5334/jors.bx>.
- [36] C.F. Dunant, K.L. Scrivener, Effects of uniaxial stress on alkali–silica reaction induced expansion of concrete, *Cem. Concr. Res.* 42 (2012) 567–576. <https://doi.org/10.1016/j.cemconres.2011.12.004>.
- [37] Z.P. Bažant, J.-C. Chern, W. Thonguthai, Finite element program for moisture and heat transfer in heated concrete, *Nucl. Eng. Des.* 68 (1982) 61–70. [https://doi.org/10.1016/0029-5493\(82\)90040-1](https://doi.org/10.1016/0029-5493(82)90040-1).
- [38] Z.P. Bazant, W. Thonguthai, PORE PRESSURE AND DRYING OF CONCRETE AT HIGH TEMPERATURE, *ASCE J Eng Mech Div.* 104 (1978) 1059–1079.
- [39] Z.P. Bažant, W. Thonguthai, Pore pressure in heated concrete walls: theoretical prediction, *Mag. Concr. Res.* 31 (1979) 67–76. <https://doi.org/10.1680/mac.1979.31.107.67>.
- [40] N. Saklani, Implementation of a Coupled Creep Damage Model in Moose Finite Element Framework: Application to Irradiated Concrete Structures, Ph.D., Arizona State University, 2020. <https://search.proquest.com/docview/2407595866/abstract/83122B70BA0C4ADDPQ/1> (accessed July 6, 2020).
- [41] H.K. Hilsdorf, J. Kropp, H.J. Koch, The Effects of Nuclear Radiation on the Mechanical Properties of Concrete, *Spec. Publ.* 55 (1978) 223–254. <https://doi.org/10.14359/6616>.
- [42] B.D. Lubachevsky, F.H. Stillinger, Geometric properties of random disk packings, *J. Stat. Phys.* 60 (1990) 561–583.
- [43] W.R. Quadros, K. Shimada, S.J. Owen, Skeleton-based computational method for the generation of a 3D finite element mesh sizing function, *Eng. Comput.* 20 (2004) 249–264. <https://doi.org/10.1007/s00366-004-0292-4>.
- [44] V.K.R. Kodur, T.C. Wang, F.P. Cheng, Predicting the fire resistance behaviour of high strength concrete columns, *Cem. Concr. Compos.* 26 (2004) 141–153. [https://doi.org/10.1016/S0958-9465\(03\)00089-1](https://doi.org/10.1016/S0958-9465(03)00089-1).
- [45] H.M. Künzle, Simultaneous heat and moisture transport in building components: one- and two-dimensional calculation using simple parameters, IRB Verlag, Stuttgart, 1995.
- [46] Z.P. Bažant, L.J. Najjar, Drying of concrete as a nonlinear diffusion problem, *Cem. Concr. Res.* 1 (1971) 461–473. [https://doi.org/10.1016/0008-8846\(71\)90054-8](https://doi.org/10.1016/0008-8846(71)90054-8).
- [47] R. Mensi, P. Acker, A. Attolou, Séchage du béton: analyse et modélisation, *Mater. Struct.*

- 21 (1988) 3–12. <https://doi.org/10.1007/BF02472523>.
- [48] A. Ababneh, F. Benboudjema, Y. Xi, Chloride Penetration in Nonsaturated Concrete, *J. Mater. Civ. Eng.* 15 (2003) 183–191. [https://doi.org/10.1061/\(ASCE\)0899-1561\(2003\)15:2\(183\)](https://doi.org/10.1061/(ASCE)0899-1561(2003)15:2(183)).
- [49] T.C. Powers, T.L. Brownyard, Studies of the Physical Properties of Hardened Portland Cement Paste, *J. Proc.* 43 (1946) 249–336. <https://doi.org/10.14359/15301>.
- [50] J.M. de Burgh, S.J. Foster, Influence of temperature on water vapour sorption isotherms and kinetics of hardened cement paste and concrete, *Cem. Concr. Res.* 92 (2017) 37–55. <https://doi.org/10.1016/j.cemconres.2016.11.006>.
- [51] I. Maruyama, G. Igarashi, Water Vapor Adsorption Isotherm Model of Portland Cement Paste, *J. Struct. Constr. Eng. Trans. AIJ.* 76 (2011) 1033–1041. <https://doi.org/10.3130/aijs.76.1033>.
- [52] V. Baroghel-Bouny, Water vapour sorption experiments on hardened cementitious materials: Part I: Essential tool for analysis of hygral behaviour and its relation to pore structure, *Cem. Concr. Res.* 37 (2007) 414–437. <https://doi.org/10.1016/j.cemconres.2006.11.019>.
- [53] S. Tada, K. Watanabe, Dynamic determination of sorption isotherm of cement based materials, *Cem. Concr. Res.* 35 (2005) 2271–2277. <https://doi.org/10.1016/j.cemconres.2005.01.002>.
- [54] D. Snoeck, L.F. Velasco, A. Mignon, S. Van Vlierberghe, P. Dubruel, P. Lodewyckx, N. De Belie, The influence of different drying techniques on the water sorption properties of cement-based materials, *Cem. Concr. Res.* 64 (2014) 54–62. <https://doi.org/10.1016/j.cemconres.2014.06.009>.
- [55] V. Baroghel-Bouny, M. Thiéry, X. Wang, Modelling of isothermal coupled moisture–ion transport in cementitious materials, *Cem. Concr. Res.* 41 (2011) 828–841. <https://doi.org/10.1016/j.cemconres.2011.04.001>.
- [56] S. Poyet, Experimental investigation of the effect of temperature on the first desorption isotherm of concrete, *Cem. Concr. Res.* 39 (2009) 1052–1059. <https://doi.org/10.1016/j.cemconres.2009.06.019>.
- [57] S. Brunauer, J. Skalny, E.E. Bodor, Adsorption on nonporous solids, *J. Colloid Interface Sci.* 30 (1969) 546–552. [https://doi.org/10.1016/0021-9797\(69\)90423-8](https://doi.org/10.1016/0021-9797(69)90423-8).
- [58] R.B. Anderson, Modifications of the Brunauer, Emmett and Teller Equation¹, *J. Am. Chem. Soc.* 68 (1946) 686–691. <https://doi.org/10.1021/ja01208a049>.
- [59] C. van den Berg, Vapour sorption equilibria and other water-starch interactions : a physico-chemical approach, (1981). <https://research.wur.nl/en/publications/vapour-sorption->

- equilibria-and-other-water-starch-interactions-a- (accessed June 3, 2020).
- [60] Y. Le Pape, J. Sanahuja, M.H.F. Alsaïd, Irradiation-induced damage in concrete-forming aggregates: revisiting literature data through micromechanics, *Mater. Struct.* 53 (2020) 62. <https://doi.org/10.1617/s11527-020-01489-6>.
- [61] M. Avrami, Granulation, Phase Change, and Microstructure Kinetics of Phase Change. III, *J. Chem. Phys.* 9 (1941) 177–184. <https://doi.org/10.1063/1.1750872>.
- [62] D.C. McDowall, The effect of gamma irradiation on the creep properties of concrete, (1972). http://inis.iaea.org/Search/search.aspx?orig_q=RN:4042786 (accessed March 19, 2020).
- [63] B. Gray, The effect of reactor radiation on cements and concrete, *Comm Eur. Communities Luxemb.* (1972) 17–39.
- [64] Z.P. Bažant, S. Baweja, Justification and refinements of model B3 for concrete creep and shrinkage 2. Updating and theoretical basis, *Mater. Struct.* 28 (1995) 488–495. <https://doi.org/10.1007/BF02473171>.
- [65] Q. Zhang, R. Le Roy, M. Vandamme, B. Zuber, Long-term creep properties of cementitious materials: Comparing microindentation testing with macroscopic uniaxial compressive testing, *Cem. Concr. Res.* 58 (2014) 89–98. <https://doi.org/10.1016/j.cemconres.2014.01.004>.
- [66] B.T. Tamtsia, J.J. Beaudoin, Basic creep of hardened cement paste A re-examination of the role of water, *Cem. Concr. Res.* 30 (2000) 1465–1475. [https://doi.org/10.1016/S0008-8846\(00\)00279-9](https://doi.org/10.1016/S0008-8846(00)00279-9).
- [67] A.B. Giorla, C.F. Dunant, Microstructural effects in the simulation of creep of concrete, *Cem. Concr. Res.* 105 (2018) 44–53. <https://doi.org/10.1016/j.cemconres.2017.12.001>.
- [68] Z.C. Grasley, D.A. Lange, Thermal dilation and internal relative humidity of hardened cement paste, *Mater. Struct.* 40 (2007) 311–317. <https://doi.org/10.1617/s11527-006-9108-x>.
- [69] I. Maruyama, G. Igarashi, Numerical Approach towards Aging Management of Concrete Structures: Material Strength Evaluation in a Massive Concrete Structure under One-Sided Heating, *J. Adv. Concr. Technol.* 13 (2015) 500–527. <https://doi.org/10.3151/jact.13.500>.
- [70] N. Neithalath, B. Pease, E. Attiogbe, Considering moisture gradients and time-dependent crack growth in restrained concrete elements subjected to drying, *Proc. Indo-US Workshop High Perform. Cem. Based Concr. Compos. Am. Ceram. Soc. Chennai India.* (2005) 11.
- [71] I. Maruyama, J. Rymeš, Temperature Dependency of Short-Term Length-Change and Desorption Isotherms of Matured Hardened Cement, *J. Adv. Concr. Technol.* 17 (2019) 188–194.

<https://doi.org/10.3151/jact.17.188>.

- [72] J. Weerheijm, J.C.A.M. Van Doormaal, Tensile failure of concrete at high loading rates: New test data on strength and fracture energy from instrumented spalling tests, *Int. J. Impact Eng.* 34 (2007) 609–626. <https://doi.org/10.1016/j.ijimpeng.2006.01.005>.
- [73] Z.P. Bažant, R. Gettu, Rate effects and load relaxation in static fracture of concrete, *ACI Mater. J.* 89 (1992) 457–468.
- [74] S. Fichant, C. La Borderie, G. Pijaudier-Cabot, Isotropic and anisotropic descriptions of damage in concrete structures, *Mech. Cohesive-Fract. Mater.* 4 (1999) 339–359. [https://doi.org/10.1002/\(SICI\)1099-1484\(199907\)4:4<339::AID-CFM65>3.0.CO;2-J](https://doi.org/10.1002/(SICI)1099-1484(199907)4:4<339::AID-CFM65>3.0.CO;2-J).
- [75] M. Kurumatani, K. Terada, J. Kato, T. Kyoya, K. Kashiya, An isotropic damage model based on fracture mechanics for concrete, *Eng. Fract. Mech.* 155 (2016) 49–66. <https://doi.org/10.1016/j.engfracmech.2016.01.020>.
- [76] J.H.P. de Vree, W.A.M. Brekelmans, M.A.J. van Gils, Comparison of nonlocal approaches in continuum damage mechanics, *Comput. Struct.* 55 (1995) 581–588. [https://doi.org/10.1016/0045-7949\(94\)00501-S](https://doi.org/10.1016/0045-7949(94)00501-S).
- [77] A.B. Giorla, Implementation of concrete creep model in grizzly, Technical Report No ORNL/TM-2017/729, 2017.
- [78] H. Huang, B.W. Spencer, G. Cai, GRIZZLY Model of Multi-Reactive Species Diffusion, Moisture/Heat Transfer and Alkali-Silica Reaction for Simulating Concrete Aging and Degradation, Idaho National Lab. (INL), Idaho Falls, ID (United States), 2015. <https://doi.org/10.2172/1244622>.
- [79] I. Maruyama, H. Sasano, Y. Nishioka, G. Igarashi, Strength and Young's modulus change in concrete due to long-term drying and heating up to 90°C, *Cem. Concr. Res.* 66 (2014) 48–63. <https://doi.org/10.1016/j.cemconres.2014.07.016>.
- [80] E. Kröner, Bounds for effective elastic moduli of disordered materials, *J. Mech. Phys. Solids.* 25 (1977) 137–155. [https://doi.org/10.1016/0022-5096\(77\)90009-6](https://doi.org/10.1016/0022-5096(77)90009-6).
- [81] I. Maruyama, A. Teramoto, G. Igarashi, Strain and thermal expansion coefficients of various cement pastes during hydration at early ages, *Mater. Struct.* 47 (2014) 27–37. <https://doi.org/10.1617/s11527-013-0042-4>.
- [82] M. Lin, M. Itoh, I. Maruyama, Mechanism of Change in Splitting Tensile Strength of Concrete during Heating or Drying up to 90°C, *J. Adv. Concr. Technol.* 13 (2015) 94–102. <https://doi.org/10.3151/jact.13.94>.
- [83] S. Djaknoun, E. Ouedraogo, A.A. Benyahia, Fracture energy of high performance mortar

- subjected to high temperature, (2010) 6.
- [84] A. Menou, G. Mounajed, H. Boussa, A. Pineaud, H. Carre, Residual fracture energy of cement paste, mortar and concrete subject to high temperature, *Theor. Appl. Fract. Mech.* 45 (2006) 64–71. <https://doi.org/10.1016/j.tafmec.2005.11.007>.
- [85] T.C. Hansen, Influence of Aggregate and Voids on Modulus of Elasticity of Concrete, Cement Mortar, and Cement Paste, *J. Proc.* 62 (1965) 193–216. <https://doi.org/10.14359/7686>.
- [86] U.J. Counto, The effect of the elastic modulus of the aggregate on the elastic modulus, creep and creep recovery of concrete, *Mag. Concr. Res.* 16 (1964) 129–138. <https://doi.org/10.1680/mac.1964.16.48.129>.
- [87] J.D. Eshelby, R.E. Peierls, The elastic field outside an ellipsoidal inclusion, *Proc. R. Soc. Lond. Ser. Math. Phys. Sci.* 252 (1959) 561–569. <https://doi.org/10.1098/rspa.1959.0173>.
- [88] J.D. Eshelby, R.E. Peierls, The determination of the elastic field of an ellipsoidal inclusion, and related problems, *Proc. R. Soc. Lond. Ser. Math. Phys. Sci.* 241 (1957) 376–396. <https://doi.org/10.1098/rspa.1957.0133>.